Study of a Stall Cell using Stereo Particle Image Velocimetry

Marinos Manolesos[1, a], Spyros G. Voutsinas[1]

[1]Laboratory of Aerodynamics, National Technical University of Athens, 9 Heroon Polytechneiou str., 15780 Athens, Greece.

The structure of Stall Cells (SCs) on wings is analyzed on the basis of Stereo PIV measurements. All experiments regard a Reynolds number 0.87×10^6 flow around a rectangular wing with endplates and an aspect ratio of 2.0. The inherently unstable Stall Cell is stabilized by means of a localized spanwise disturbance. Velocity, vorticity and Reynolds stress data above the wing and in the wake are presented and discussed, also in combination with CFD data. The present study completes and clarifies the previously suggested models regarding the SC structure. The SC emerges in between the separation and trailing edge shear layer where three different types of vortices are identified: (a) the Stall Cell vortices that start normal to the wing surface and continue downstream aligned with the free stream, (b) the Separation Line Vortex and (c) the Trailing Edge Line Vortex that both run parallel to the wing trailing edge and grow significantly at the center of the Stall Cell. Analysis of the Reynolds stress data reveals high anisotropy. Concentration of high streamwise shear stress values is connected to the two shear layers and high cross shear Reynolds stresses are connected to vortex stretching. High normal Reynolds stress values are observed a) in the separation but not in the trailing edge shear layer indicating the flapping of the former and b) along the Stall Cell vortices indicating their wandering motion. The eddy viscosity based RANS simulations are found in good qualitative agreement with the experiments in terms of the type and position of the identified vortex structures, an agreement which is linked to the correct trend in the predicted shear Reynolds stresses distributions. Quantitative deviations of the numerical results from the measurements are attributed to the isotropic definition of the turbulence model. Therefore, use of Large Eddy Simulation is suggested for better prediction of the flow.

I. INTRODUCTION

Wind tunnel testing of rectangular wing models has been the main way to obtain steady airfoil polar curves for decades. The standard procedure is to deduce lift from surface pressure measurements at mid-span and drag from wake rake data. Suction at the sidewalls or endplates are employed in order to minimize corner flow effects. Such a procedure is

[a]Author to whom correspondence should be addressed. Electronic mail: marinos@fluid.mech.ntua.gr, Tel: +30 6932 401959, Fax: +30 210 7721057

based on the assumption that the flow at the center of the wing remains two-dimensional as long as the wing aspect ratio is large enough; this, despite the fact that from early on questions had been raised regarding the validity of such tests under separated flow conditions [1]. In fact numerous airfoils have been reported to experience three-dimensional separation and more specifically Stall Cell (SC) formation [2]–[7]. SCs are large scale structures of separated flow that consist of a pair of counter rotating vortices. Apart from rectangular wind tunnel models, SCs have also been observed on swept cantilevered wings [8] and on airplane wings [9], [10].

SCs are formed on the suction side of airfoils that experience trailing edge (TE) type stall or a combination of leading edge and TE type stall at angles of attack around maximum lift, as Broeren & Bragg [7] found in their extensive study. Although they have been known for a long time (e.g. [11]) our knowledge about their behavior, structure and formation mechanisms remains limited.

The present investigation on SCs has been originally motivated by the possible implications to the design of wind turbine blades and justified for the following two reasons. First, SCs have been reported on wind tunnel models of airfoils designed for or used on wind turbine blades [5], [12] and, second, recent studies report on the formation of SCs on wind turbine blades at standstill [13]. The latter point becomes even more important considering that SCs have been linked to wing buffeting [8]. Otherwise the work reported is of generic character and aims at improving the current understanding on SCs.

To this end, a combined experimental and computational investigation was launched at the National Technical University of Athens (NTUA). Geometrical characterization of SCs using tuft flow visualization data was presented in [14] whereas pressure data and Reynolds Averaged Navier-Stokes (RANS) simulations using eddy-viscosity turbulence modeling were compared in [15]. The present paper complements and extends the previous work by providing an in depth study of the flow associated with SCs by means of a Stereo Particle Image Velocimetry (Stereo PIV) campaign and discusses issues related to their prediction.

In the rest of this paper, first a short survey on previous research on SCs is given, focusing mainly on the SC structure description (see [16] for a more detailed literature review). Next, the experimental set up of the present campaign is described followed by the presentation and discussion of the results. Flow field surveys above the wing surface and in the wake are analyzed and vortex structures are identified. Further insight in the underlying flow mechanisms is retrieved by analyzing the Reynolds (Re) stresses and by correlating CFD predictions with the measured data. Finally, a synthesis of the present study findings along with those from previous investigations is given in the final section.

Notation conventions: Throughout this paper the spanwise coordinate is non-dimensionalized with the wing span (S), Z = z/S, and ranges from -0.5 to 0.5. Accordingly, the non-dimensional chordwise coordinate is X = x/c, where c is the wing chord and X = 1.0 is at the wing TE. The vertical coordinate is Y = y/c, with Y = 0.0 at the wing TE. Velocity components, u, v, w, and Reynolds stresses are normalized with the free stream velocity U_∞ e.g. $U = \overline{u} / U_\infty$ and $\overline{U'U'} = \overline{u'u'} / U_\infty^2$, while normalized vorticity is the streamwise vorticity:

$\omega c / U_\infty$. The spanwise vorticity ω_z is also normalized by c / U_∞ . Q symbolizes the second invariant of the velocity gradient tensor, $\nabla \boldsymbol{u}$, while S and Ω are as the symmetric and antisymmetric components of $\nabla \boldsymbol{u}$, as detailed in the text. St is the Strouhal number defined as $St = f \cdot c \cdot \sin\alpha / U_\infty$, where f is the measured frequency and α is the angle of attack.

A. Previous works

1. Wall effects, unsteadiness and generation mechanism

The onset of SCs has been reported on wings with free tips [2], on wings with endplates [3], on wall-to-wall models with or without suction [1] and on cantilevered wings with a single free tip [8]. In a different study [17] SCs were found to be "resistant" against various sidewall treatments. In fact, no known wall condition or treatment has been reported to prevent SC formation. In addition, side wall proximity does not seem to be the cause of SC formation, since they have been reported on wings with aspect ratio (AR) values ranging from AR = 1.5 (in [5], [14]) to AR = 12 (in [2]). These studies suggest that even though their number or behavior may be affected by the model AR and the conditions at the tip or by wall proximity, the generating mechanism does not result from either of the two.

In most cases, SCs are unsteady coherent structures. In various studies they have been reported to form/disappear in a seemingly random manner and/or move in the spanwise direction [1], [3], [8], [18]. However, Broeren & Bragg [7] and Elimelech et al. [19] in their experiments in low Turbulence Intensity (T.I. < 0.15%) and relatively low Re number (30×10^4 in [7] and 1-2 10^4 in [19]) reported no spanwise movement or substantial unsteadiness of the SCs. To the authors' best knowledge the time varying behavior of SCs at higher Re numbers has not been correlated to flow Re number, wing AR or angle of attack. Whether low T.I. in [7] and [19] in connection with low Re is responsible for the suppression of the SC unsteadiness is not clear.

Regarding the generating mechanism of SCs, Rodriguez & Theofilis, in their global instability study [20], attributed the generation of SCs to the amplification of a spanwise disturbance and connect the onset of SCs to sufficiently large disturbance amplitude. In accordance to the above statement, Elimelech et al. [19] showed that the amplification of a two-dimensional perturbation could not justify the formation of structures of such a large scale as the SCs and that SCs could be only explained as result of a spanwise 3D perturbation.

2. Computational studies

While numerous extensive experimental studies regarding SCs have been published in the past, the number of detailed computational investigations on SCs remains small ([6], [15], [17], [18], [20]) and not all of the published studies manage to reproduce the experimentally observed SCs in their 3D RANS calculations. In these studies multiple terms are used when referring to SCs, e.g. "mushroom-shaped" or "owl's eyes" structures or simply "three-dimensional separation", however, they all deal with the same phenomenon.

3D RANS simulations constitute the mostly used approach to predict SCs, despite the fact that turbulence and transition modeling remain important issues. The basic rationale in using 3D RANS is their wide use in engineering applications and the need to assess their ability to cost effectively predict aerodynamic loads in separated flow conditions.

In [17], [18], it was found that on a wing of finite AR, the numerically predicted 3D structure of separated flow does not depend on the choice of eddy viscosity model (in [18] the k-ω - SST [22] and Spalart-Allmaras [23] turbulence models were used, while in [17] the k-ω - Wilcox model [24] was additionally applied). In [6], [21] 2D RANS, 3D RANS and 3D Detached Eddy Simulation (DES) predictions were compared to experimental pressure data. It was found that: all models had difficulty to consistently predict lift and drag in stalled conditions; 3D RANS simulations using the k-ω SST model were in better agreement with measurements than those of 3D DES at angles of attack around maximum lift; well-formed SCs on the wing surface were predicted in the 3D RANS simulated flow while in the 3D DES simulations the flow patterns appeared chaotic.

Publications using LES modeling of SCs were not found. With respect to other numerical studies, of some relevance to SCs is the work by Taira & Colonius [25] who used an immersed boundary method to consider the case of a flat plate wing ($1 \leq AR \leq 4$) in deep stall at Re = 300 and Re = 500. Besides the very low Re number and the flat plate profile, the specific set-up is strongly affected by the presence of tip vortices that increase in intensity with the angle of attack which ranged from $\alpha = 0°$ up to $\alpha = 60°$. So its relevance with the present case is limited. However, cellular structures similar to SCs were found for AR = 2 and 4 but not for AR = 1 suggesting that a minimum AR is necessary for a SC to develop.

3. Stall cell structure

Regarding the SC structure various models have been proposed in the past. Initially Winkelmann & Barlow [2] proposed a "tentative flow model" according to which a "loop vortex" connected to the two focal points on the wing surface and a secondary vortex of opposite vorticity ran along the wing TE. Weihs & Katz [26] on the other hand, postulated that the time averaged flow over a SC is a 3D vortex ring that hits the wing surface at the two foci. Later, Yon & Katz [3] based on pressure measurements indicated that no loop vortex exists and that two counter rotating vortices start from the surface foci and then extend downstream aligned with the flow. The same investigators [3] also claimed that no concentrated spanwise vortex exists.

A similar surface flow pattern was obtained in the global stability analysis by Rodriguez & Theofilis [20] where a 2D profile in steady stall at Re = 200 was subjected to a spanwise disturbance. For the most unstable mode, two levels of amplitude were considered. In the low amplitude case a wavy distortion of the trailing vortex appears which, however, remains parted from the separated vortex. In the high amplitude case, counter rotating foci appear on the wing surface, the trailing edge line vortex is further distorted in a sequence of open “U” shapes while the separated vortex periodically breaks and directs vorticity downstream. While the patterns in [3] and [20] agree on the existence of two counter rotating trailing vortices, in [20] it is the separation vortex that periodically brakes and bends downstream, while [3] assumes that the separation shear layer is "bounded" by the trailing vortices, which start normal to the wing surface.

The complex vortical interaction involved in 3D separation was discussed in [15] on the basis of 3D RANS simulations using the Spalart-Allmaras turbulence model. The quality of the simulations was assessed by comparing predictions to measured pressure data and was

found good. Under fully turbulent conditions, excellent predictions were obtained in for the linear part of the lift polar; the onset of separation was obtained with a ~3° delay in angle of attack leading to lift and drag deviations over this range; however, once a SC was formed in the CFD simulations, the deviations in lift and drag became smaller, closely following the trend of the measured curves.

The Q criterion [27] was used to detect the spatial development of the vortex structures, in combination with the condition that the local pressure is lower than the ambient one. Q represents the local balance between vorticity magnitude and shear strain rate and is defined as the second invariant $\nabla \boldsymbol{u}$:

$$Q \equiv 1/2 \left(u_{i,i}^2 - u_{i,j} u_{j,i} \right) = 1/2 \left(\|\Omega\|^2 - \|S\|^2 \right) \quad (1)$$

S and Ω being the symmetric and antisymmetric components of $\nabla \boldsymbol{u}$ **,** respectively:

$$S_{i,j} = 1/2 \left(u_{i,j} + u_{j,i} \right) \quad (2)$$

$$\Omega_{i,j} = 1/2 \left(u_{i,j} - u_{j,i} \right) \quad (3)$$

The selection of the Q criterion in the rest of this paper was made conformity with [15]. Nevertheless, application of the λ_2 criterion [28] to the 2D in-plane flow gave very similar results and could have equally been used.

Since the simulations in [15] were steady, the obtained flow pattern corresponds to the time averaged flow field. Within this context the following three distinct types of vortex structures were associated to the SC:

1. Two counter rotating SC vortices that start normal to the wing surface and extend downstream. Their focal points are found within the separation line.
2. The Separation Line Vortex (SLV) that runs above and parallel to the wing TE. This vortex grows at the center of the SC and extends on both sides outside the SC remaining parallel to the wing TE.
3. The Trailing Edge Line Vortex (TELV) which has vorticity of opposite sign compared to the SLV. The TELV also runs parallel to the wing TE at the sides of the SC and grows inboard of the SC vortices.

Figure 1 shows data obtained using MaPFlow, the in-house eddy-viscosity based U-RANS CFD code used in [15]. The case refers to the fully turbulent steady state simulation of a wing of AR 2.0 at α = 10° and Re number 0.87×10^6 using the Spalart-Allmaras turbulence model. Taking advantage of spanwise symmetry only half of the wing was simulated while at the position of the endplates inviscid wall boundary condition was applied.

In Figure 1-a surface flow lines on the wing suction surface along with in-plane flow lines on planes Z = 0.0 (symmetry plane), Z = -0.25 and Z = -0.5 (wing tip) are shown along with the 3D separation line, while Figure 1-c is a side view detail of the in plane flow lines on the two first planes. The SC vortex focus is clearly visible on the wing surface. In between the SC and the tip, the flow gradually tends to become two-dimensional with only a small part of

separated flow. Inside the SC, from Z = -0.25 to Z = 0.0, the SLV grows significantly, as does the TELV (see Figure 1-c).

In Figure 1-b the iso-surface Q = 1 is shown. Interpreted vortex core lines with vorticity direction are also drawn. Throughout the paper, the notion of (tube) vortices is used in order to facilitate description and understanding. In reality the flow in question is a highly complex unsteady 3D vortical flow. Vortices correspond to vorticity concentrations in Eulerian description along a line embedded in an encompassing shear layer. Furthermore, the flow shown corresponds to the final (converged) stage of the SC formation process and is time averaged; therefore information on the transient leading to the formation of the SC cannot be obtained. This also holds for the experimental results.

A brief description of the time averaged flow is as follows: The SC vortices (their axis shown in red) start normal to the wing suction surface and subsequently, under the influence of the SLV (shown in green), they are aligned with the free stream to continue downstream as streamwise vortices. At the same time they converge towards the center of the SC, so the SC width in the wake is smaller than that on the wing surface. The SLV and the TELV (shown in yellow) run parallel to the wing TE at the sides of the SC and grow in strength and size inboard of the SC vortices, at the center of the SC. The TELV takes an open “U” shape while the SLV takes an open “∩” shape.

In numerical simulations performed on larger AR wings more SCs were formed, indicating that the number of SCs depends on the width of the numerical domain and equivalently the wing AR, in conformity with various experimental studies [2]–[4], [19]. When multiple SCs form, the SLV and the TELV are continuous vortices that run along the wing span and grow at the center of the adjacent SCs. This suggests that the SC structure described earlier for a single SC holds in the case of multiple SCs as well.

The presently reported Stereo PIV investigation aims at confirming the above CFD derived description of the SC time-averaged flow by identifying the vortex structures that compose the SC; detecting their locations and detailing the flow behavior inside a SC. A detailed comparison with SC structure models proposed so far is given in the last section of the paper.

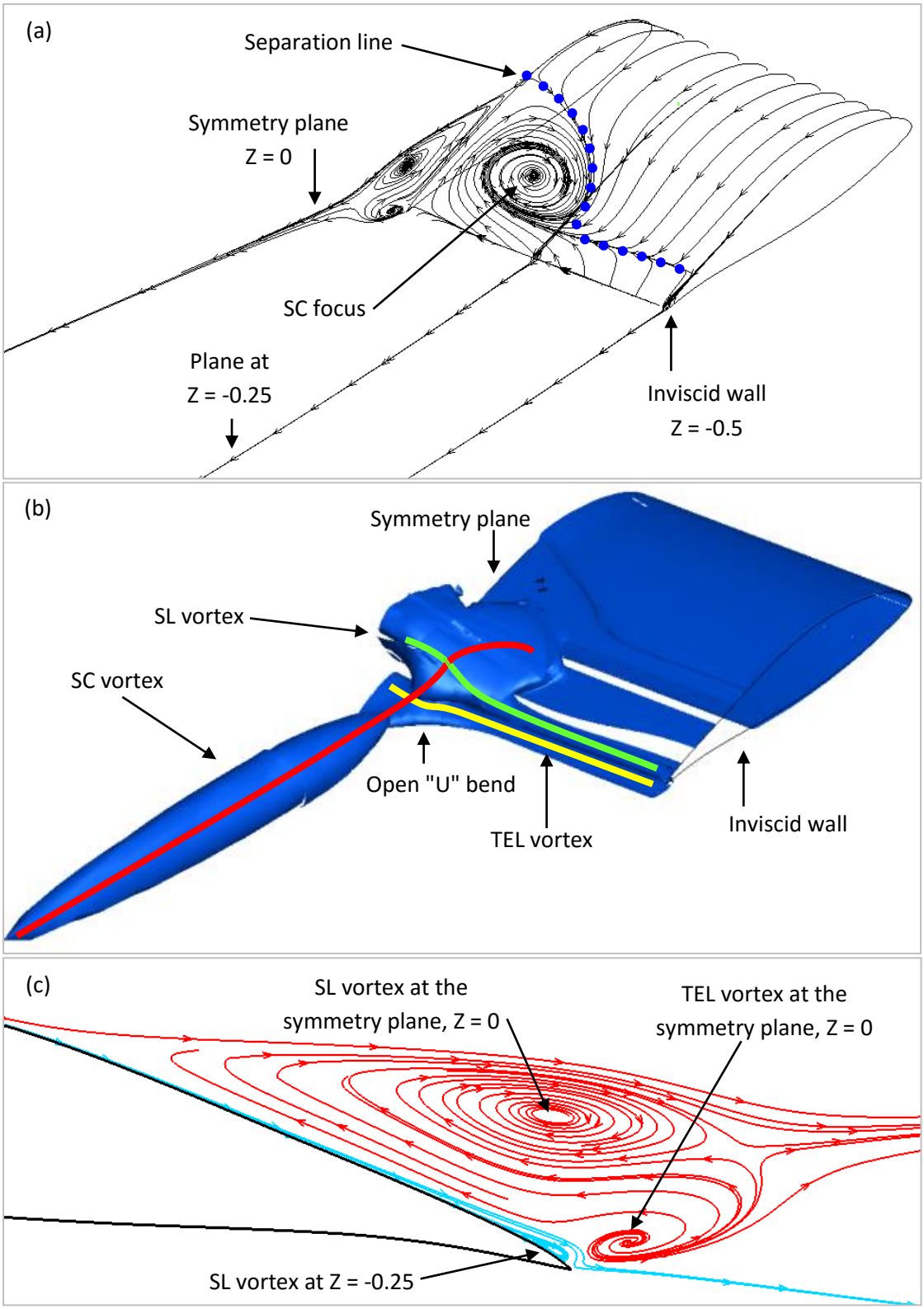

Figure 1: The CFD obtained SC structure. (a) Surface flow lines on the wing suction surface along with in-plane flow lines on planes Z = 0 (left side - symmetry plane), Z = -0.25 and Z = -0.5 (right side - inviscid wall). Blue dots indicate the 3D separation line. (b) Q=1 iso-surface. Interpreted vortex core lines with vorticity direction are also shown. The open "U" shape of the TELV inboard of the SC vortices is also indicated. (c) Side view detail of in plane flow lines on plane Z = 0 (symmetry plane - red lines) and Z = -0.25 (AR 2.0, Re = 0.87×10^6, $\alpha = 10°$).

II. EXPERIMENTAL APPROACH

A. Wind tunnel and wing model

All experiments were carried out at the 1.8m×1.4m (width × height) test section of the NTUA wind tunnel. The wind tunnel is of the closed single-return type with a total circuit length of 68.81 m. The contraction ratio is 6.45:1 and the maximum velocity 60 m/s. The free-stream turbulence level in the 3.75 m long octagonal test section is below 0.2%.

The tests concerned an 18% thick cambered airfoil optimized for use on variable pitch and variable speed multi-MW wind turbines [29]. It belongs to the flat-top type experiencing TE separation leading to gradual lift built-up and smooth post stall behavior.

The wing model had a chord of 0.6m and spanned the test section vertically in order to minimize blockage. The solid blockage of the model was 6.9% of the tunnel section at 12° angle of attack and reached a maximum of 9.2% at the highest angle, 16°, still below 10%, see [9]. The Re number for all tests was 0.87×10^6.

In order to minimize the effect of the wind tunnel boundary layer, side fences were used (Figure 2). The fences were made of Plexiglas and could move along the model span so the AR of the model could vary. All data in this report refer to the AR = 2.0 case. It is noted at this point that the wing profile extended both inboard and outboard of the fences and, as explained in [14], tufts showed no spillage over the fences.

The 60° ZZ tape used as a localized disturbance was 0.4mm high and was located at the center of the wing suction side for only 10% of its span. It was placed at X = 0.02 so that it would always be met by laminar flow. Its height exceeds the requirements for transition at Re = 0.87×10^6, where all the tests were done. As detailed in [14] this was done deliberately as the ZZ tape is not there to trip the flow, although this happens as well, but to act as a large enough spanwise disturbance that breaks the spanwise uniformity of the flow. The ZZ tape geometry can be seen in Figure 3.

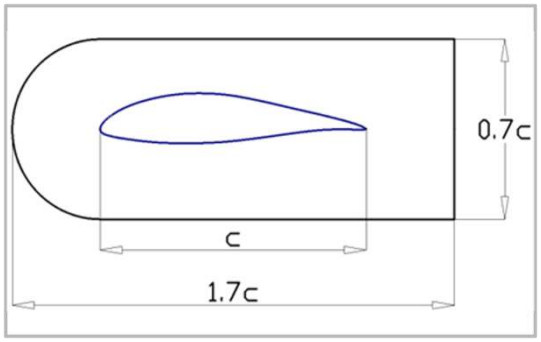

Figure 2: Fences shape and dimensions

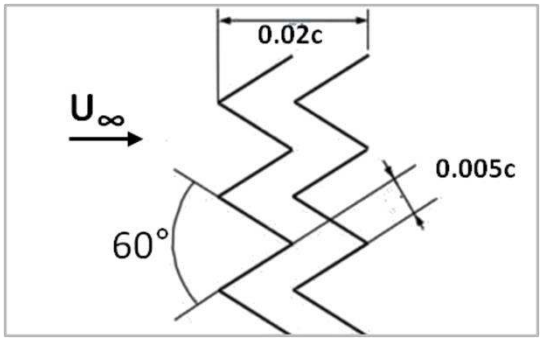

Figure 3: The zigzag tape dimensions

B. Stereo PIV set up

The Stereo-PIV equipment included a TSI 30mJ Nd:YAG PIV laser with dual cavities which produced a 2.5mm thick light sheet at the measurement position. The flow was seeded with oil droplets of 1μm mean diameter created by a commercial generator (TSI model 9307). Two TSI Powerview Plus™ 4MP Cameras were used, located inside the test section 1.2c

downstream of the TE. Depending on the size of the desired field of view, two pairs of lenses, one Nikkon 50mm f/1.8 and one Tamron 90mm f/2.8, were used. The lenses were always set at the largest aperture to allow the maximum amount of light to reach the CCD sensor.

The pulse separation time was 20μsec giving a minimum resolved velocity (the velocity corresponding to displacement of 0.1px [30], [31]) equal to $0.03U_\infty$. The error due to camera vibration was found to be an order of magnitude smaller than the minimum resolved velocity. A background image was subtracted from the measurement images to remove reflections. For planes A and B, which are above the wing surface the nearest velocity vector is at 1.3mm and 0.9mm from the wing surface, respectively. Due to strong reflections it was not possible to measure the flow closer to the surface. In total, 2000 samples were taken for each measurement frame. For this number of samples the average velocity components are measured with a 95% confidence interval of, at most, 0.9% of the free stream. For the rms quantities the corresponding confidence interval is 6.0%. A more detailed description of the PIV set up can be found in [16].

C. Stabilization of the SCs

Tuft flow visualization results [14] showed that beyond a certain angle of attack various combinations of SCs could form on the wing, e.g. a single SC travelling in the spanwise direction, two adjacent SCs jostling against each other or one full SC along with "half a SC"[b] next to the wing fence. The flow would intermittently change between these forms and no correlation of this switching behavior with angle of attack, Re number or AR was found within the range examined ($0.5\times10^6 \le Re \le 1.5\times10^6$ and $1.5 \le AR \le 2.0$).

In order to investigate the SC structure it was necessary to suppress the unsteady character of the flow. In [14] it was shown that it is possible to stabilize a SC at the center of a wing using a zigzag (ZZ) tape as a localized disturbance. It is noted that placing the ZZ tape over the whole span had no stabilizing effect, while placing the ZZ tape over the two sides of the model and leaving its center free led to the formation of two half SCs adjacent to the fences. The localized disturbance was finally located at the center of the wing span for symmetry reasons. The localized disturbance forced the flow to select one of the possible modes for the specific AR. In particular, a stable SC was formed at the center of the wing, which did not traverse along the wing span. It was also found that, compared to the case without the localized disturbance, for high enough angles of attack and for Re numbers ranging from 0.5×10^6 to 1.5×10^6, the ZZ tape did not affect the SC size or the chordwise and spanwise length of the separated flow area, as this was measured based on tuft flow visualization results. In the present investigation the case of the stabilized SC is considered at $\alpha = 10°$ and $Re = 0.87\times10^6$.

It is emphasized that while the ZZ tape has a stabilizing effect on SCs, it does not trigger its formation. Adding a localized disturbance prevents the SC from moving in the spanwise

[b] Half a SC is a structure where only one SC vortex appears next to the fence forming a "full SC" together with its mirror vortex with respect to the fence wall.

direction and locks the flow to the formation of a single SC, on a wing where SCs would form with or without the ZZ tape.

D. Stereo PIV measurement planes

In order to capture the complex three-dimensional structure inside the SC, measurements were taken on three planes normal to the flow (labeled A, B and C), and five planes normal to the wing span (labeled α, β, γ, δ and ε). A side view of the measurement planes is shown in Figure 4. A schematic planform view of the test set up is given in Figure 5.

Guidance in choosing the placement of the measuring planes was given by the oil flow pattern on the wing suction side, shown in Figure 6. The flow is from left to right, but the wing front part is not included in the picture for greater detail. As the wing is located vertically in the tunnel, gravity affects the final pattern by pulling the oil mix downwards at areas of low velocity. Still, the SC structure is clearly visible. The surface foci of the SC vortices are located approximately at Z = ±0.130 with respect to the wing mid span (Z = 0.0). Their chordwise location is X ≈ 0.91 and the most upstream point of the SC is at X ≈ 0.48. The thick red vertical lines in the figure indicate the location of the three measurement planes normal to the flow at chordwise locations 0.6c (plane A), 0.8c (plane B) and 1.06c (plane C). The spanwise locations of planes α to ε, which are located normal to the wing span, are given by the thick white lines in Figure 6. Note that these planes are downstream of the wing TE, see Figure 4 and Figure 5. The exact positions of all planes are given in Table I.

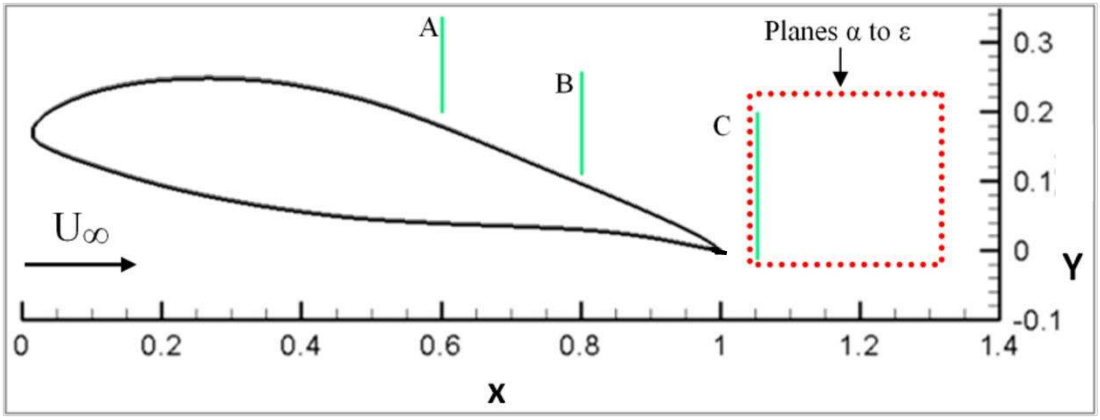

Figure 4: Stereo PIV measurement planes. Planes normal to the flow (A, B and C) are shown with solid green line. The red dotted line shows the planes normal to the wing span (α, β, γ, δ and ε).

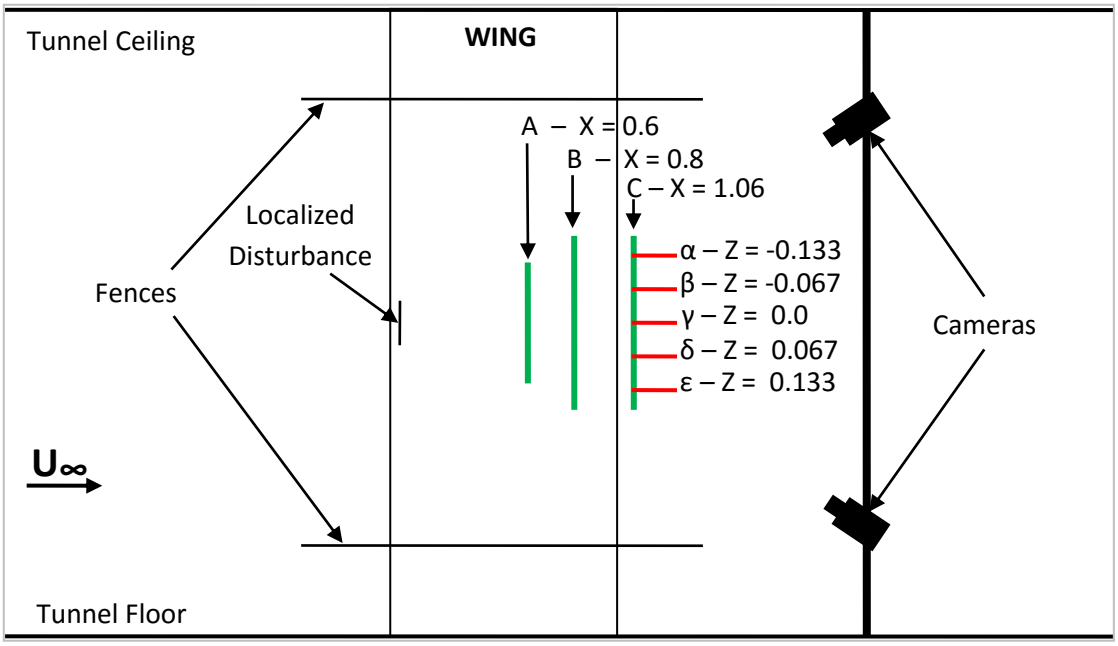

Figure 5: Schematic planform view of the test set up. The wing, the fences, the localized disturbance and the cameras are shown along with the measurement planes. Planes normal to the flow (A, B and C) are indicated by vertical green lines, while planes normal to the wing span (α, β, γ, δ and ε) are shown with red horizontal lines. Note that planes A, B and C consisted of multiple adjacent measurement frames, which were combined together in post processing. Planes α to ε were single measurement frames.

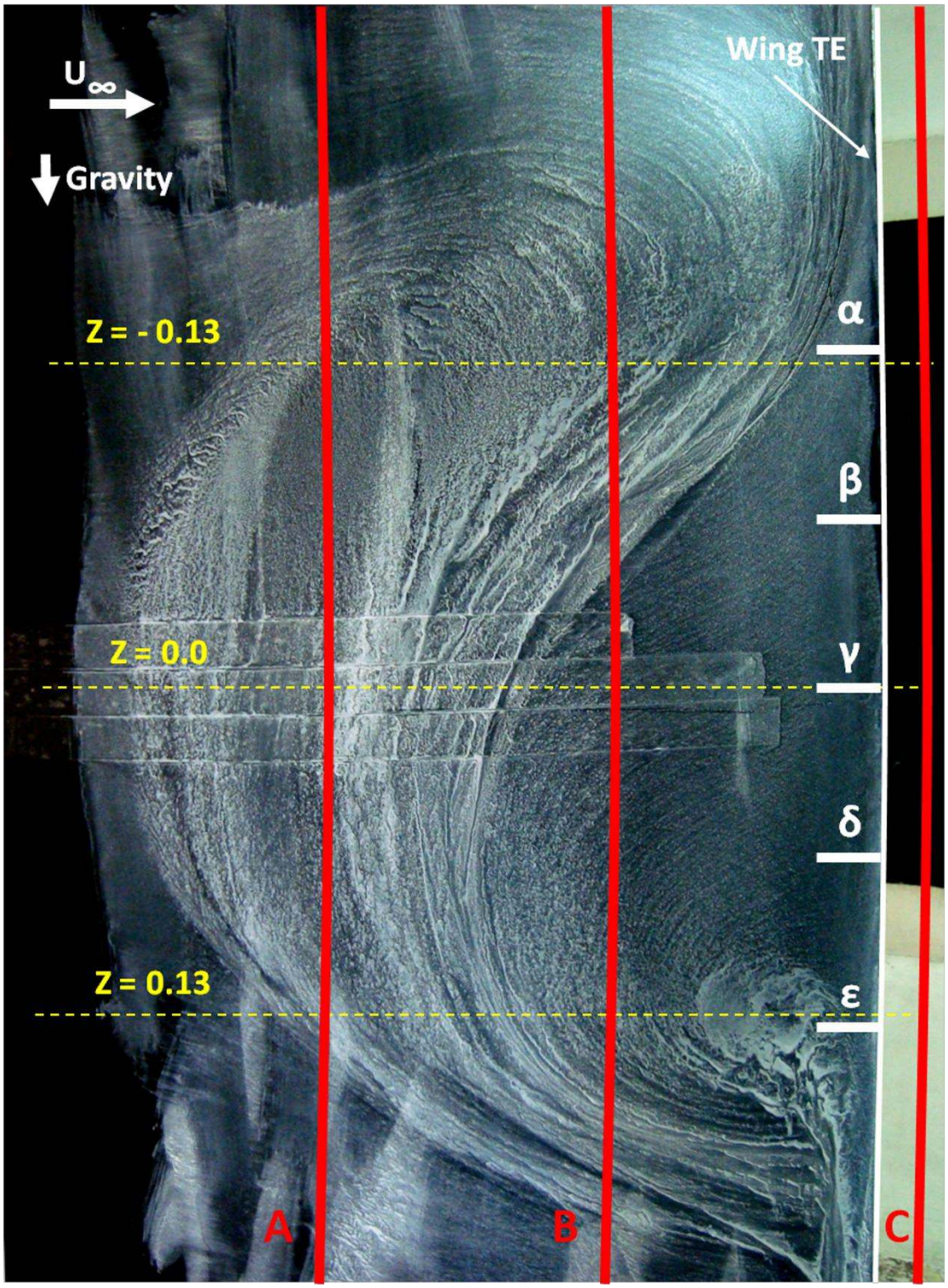

Figure 6: Oil flow pattern on the wing suction side for α = 10°, Re = 0.87×10^6. The flow is from left to right. The wing is located vertically in the tunnel and, hence, gravity is pulling the oil mix downwards, affecting the final pattern. The red solid lines indicate the measurement planes normal to the flow, A, B and C. Thick white horizontal marks indicate the spanwise position of planes normal to the wing span, α to ε. Thin dashed yellow lines indicate the wing center span (Z = 0.0) and the interpreted locations of the two SC vortex cores (Z = ±0.130). The wing TE is highlighted with a white line. The chordwise tapes at the center of the wing were used to cover the pressure taps during flow visualization.

Table I: Position of the measurement planes

Planes normal to the flow:	A		B		C
X	0.6		0.8		1.06
Planes normal to the wing span:	α	β	γ	δ	ε
Z	-0.133	-0.067	0.0	0.067	0.133

Finally, as guidance, a schematic of the expected vortex core positions with respect to the measurement planes is given in Figure 7. For clarity the figure is split in two parts. The left part (a) shows only the two counter rotating SC vortices that start normal to the wing surface and extend downstream. The SLV and the TELV which run parallel to the wing TE and also have vorticity of opposite sign are shown in the right part of the figure (b).

SCs being large scale structures, the area covered by the velocity measurements had to be of large extent, especially as regards the planes normal to the flow. For this reason, for each of the normal planes, measurements were performed in a series of adjacent frames normal to the flow with at least 20% overlapping. In the results, where the adjacent planes are patched together some small discontinuities appear, especially with regard to the vorticity contours. No smoothing was applied to the contours and since the vorticity is computed from different sets of velocity vectors exact match was not expected at the borders. Besides, the various frames were taken under the same conditions, but on different days and some small discrepancies, due to e.g. imperfect model positioning, may be expected.

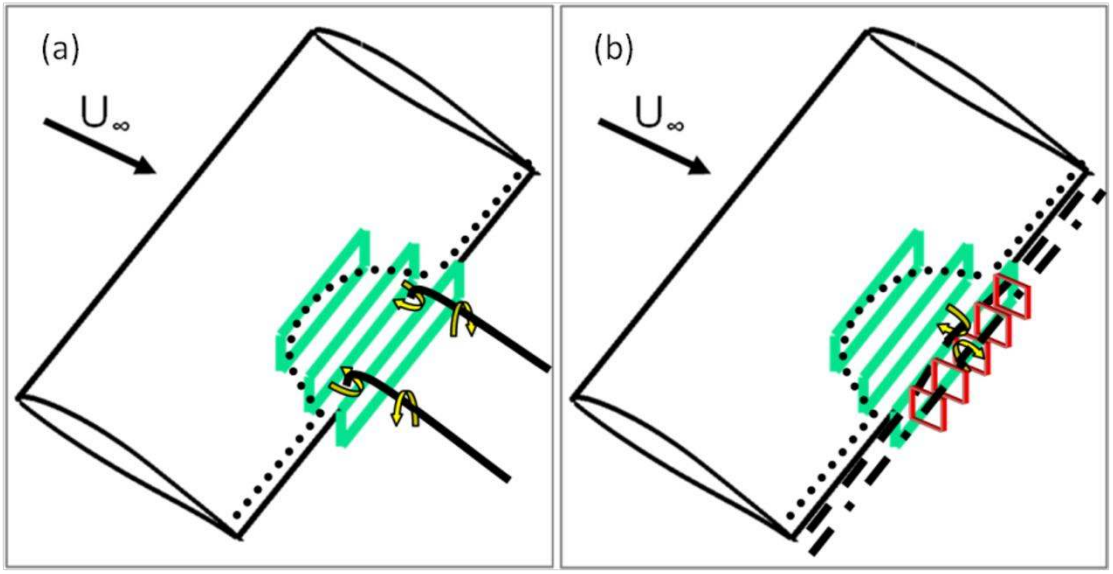

Figure 7: (a) Schematic of the SC vortices in relation to the measurement planes normal to the flow. (b) Schematic of the TELV (dashed line) and the SLV (dashed-dotted line) in relation to the measurement planes. The dotted line on the wing suction surface represents separation line. Planes normal to the flow are shown with thick green line. The thin red squares show the planes normal to the wing span where Stereo PIV data was acquired.

III. RESULTS AND DISCUSSION

In view of detailing the structure of the SC and by that also confirming the interpretation drawn from CFD simulations as pictured in Figure 1, the following steps are taken:

A. First, the velocity field inside the SC is presented focusing on the streamwise and spanwise velocity components and on in-plane flow lines.
B. Next, the vortex structures associated with the SC are identified, based on contour plots of normalized vorticity and of the Q criterion.
C. A deeper insight in the spatial development of the identified vortex structures and shear layers is obtained from the measured Reynolds stresses.
D. Finally a closer look at the correlation between computational data and experimental results follows.

A. The velocity field

An overview of the flow above the wing surface is given in Figure 8 and Figure 9, in terms of contour plots of U and W on planes A, B and C. The dashed iso-lines correspond to U = 0 and outline the region of reversed flow. The highest values of reversed flow appear on plane B, close to the wing surface between the two SC vortices. The area of reversed flow is initially very limited (plane A, X = 0.6), grows on plane B and contracts in the spanwise direction on plane C, located in the wake just downstream the TE. The spanwise contraction on plane C is driven by the significant localized increase and sign change of W (Figure 9). Along the A to C passage, the thickness of the reversed flow region and that of the surrounding shear layer increases. The spanwise contraction and the pronounced thickness increase of the reversed flow are first indications of the presence of the SC vortices.

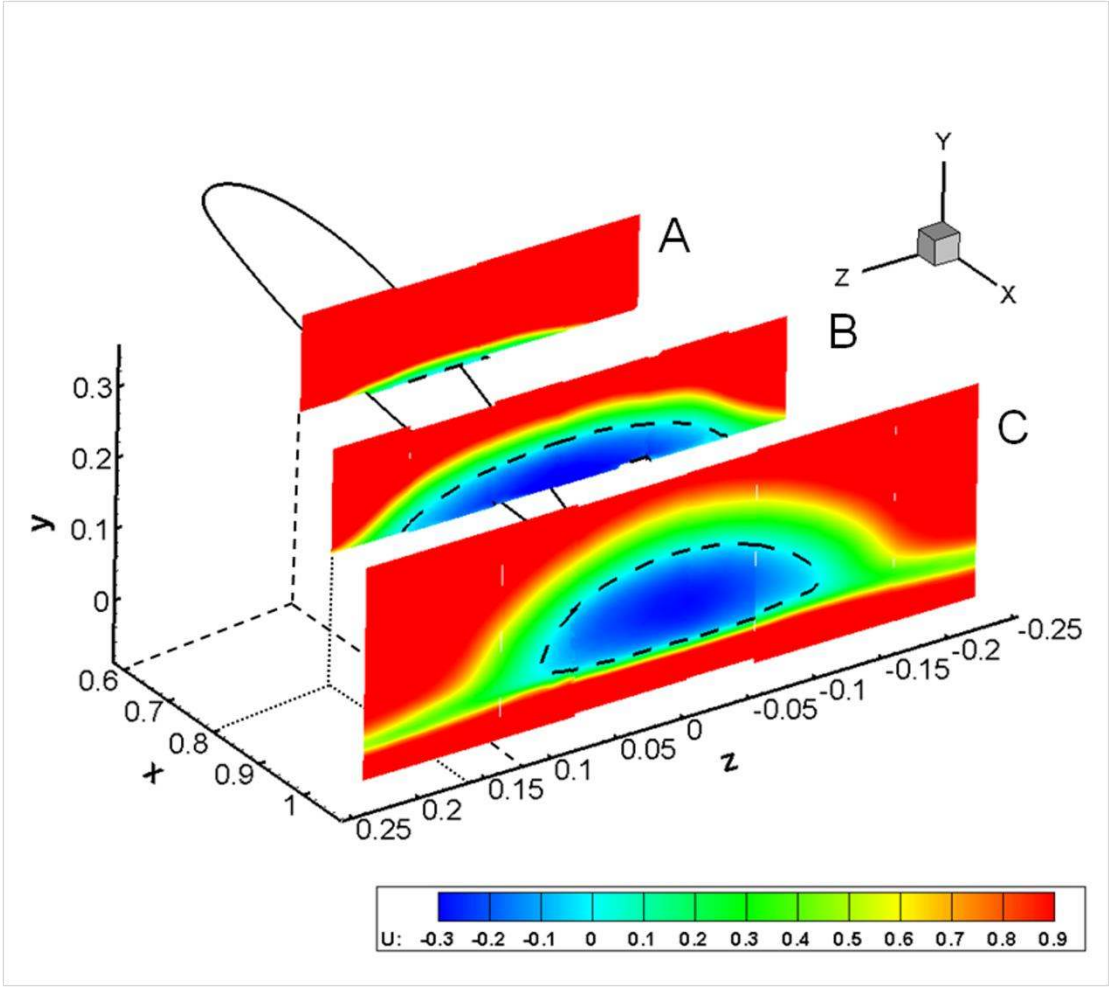

Figure 8: Contours of normalized streamwise velocity (U) at X = 0.6 (plane A), X = 0.8 (plane B) and X = 1.06 (plane C). The dashed iso-line corresponds to U = 0 (α = 10°, Re = 0.87×10^6).

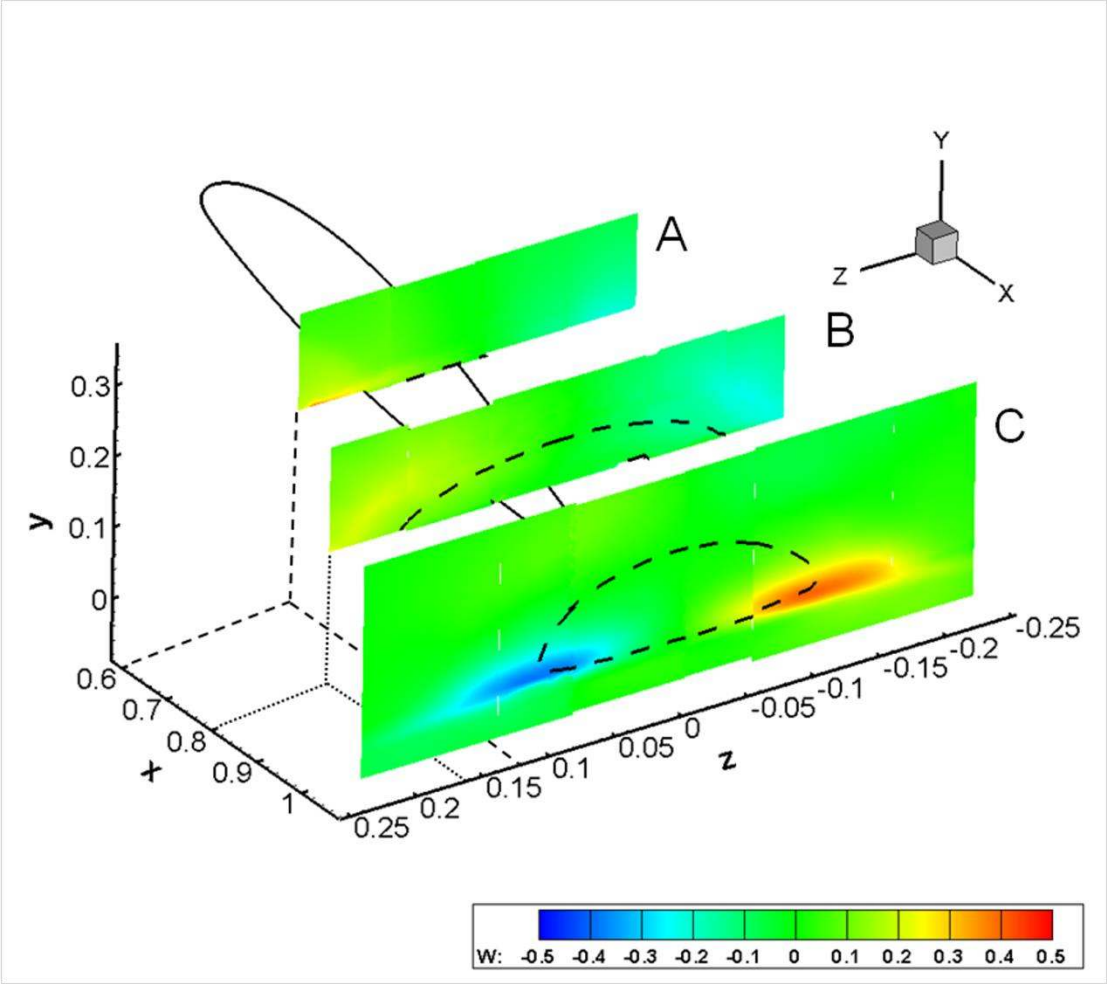

Figure 9: Contours of normalized spanwise velocity (W) at X = 0.6 (plane A), X = 0.8 (plane B) and X = 1.06 (plane C). The dashed iso-line corresponds to U = 0 (α = 10°, Re = 0.87×10^6).

In Figure 10 contours of W on planes normal to the wing span are shown together with in-plane stream lines. The areas of increased W values first observed on plane C (Figure 9) are shown here to extend downstream in the wake. The highest W values are found on planes α and ε as expected, since these planes are approximately downstream of the SC vortex cores, at Z = ±0.13, as indicated in Figure 6.

Further details of the flow in the wake region are given in Figure 11 by the W profiles at the spanwise locations of planes α, β, δ and ε. The velocity at the center of the wing span (Z = 0, plane γ) is always practically zero and is omitted. At stations Z = ±0.067 (top row), the peak in W is higher at X = 1.18 (central column) than at X = 1.06 (left column). This suggests that under mutual induction, the SC vortices are pushed upwards. On the contrary the velocity peak at Z = ±0.133 (bottom row) and X = 1.30 (right column) is lower than at X = 1.18 (central column). It is conceivable that this happens due to the downwash created by the SC vortices in that region, as they move towards the centre of the SC in the wake. The inboard movement of the SC vortices is discussed in the Reynolds stress section and in [15].

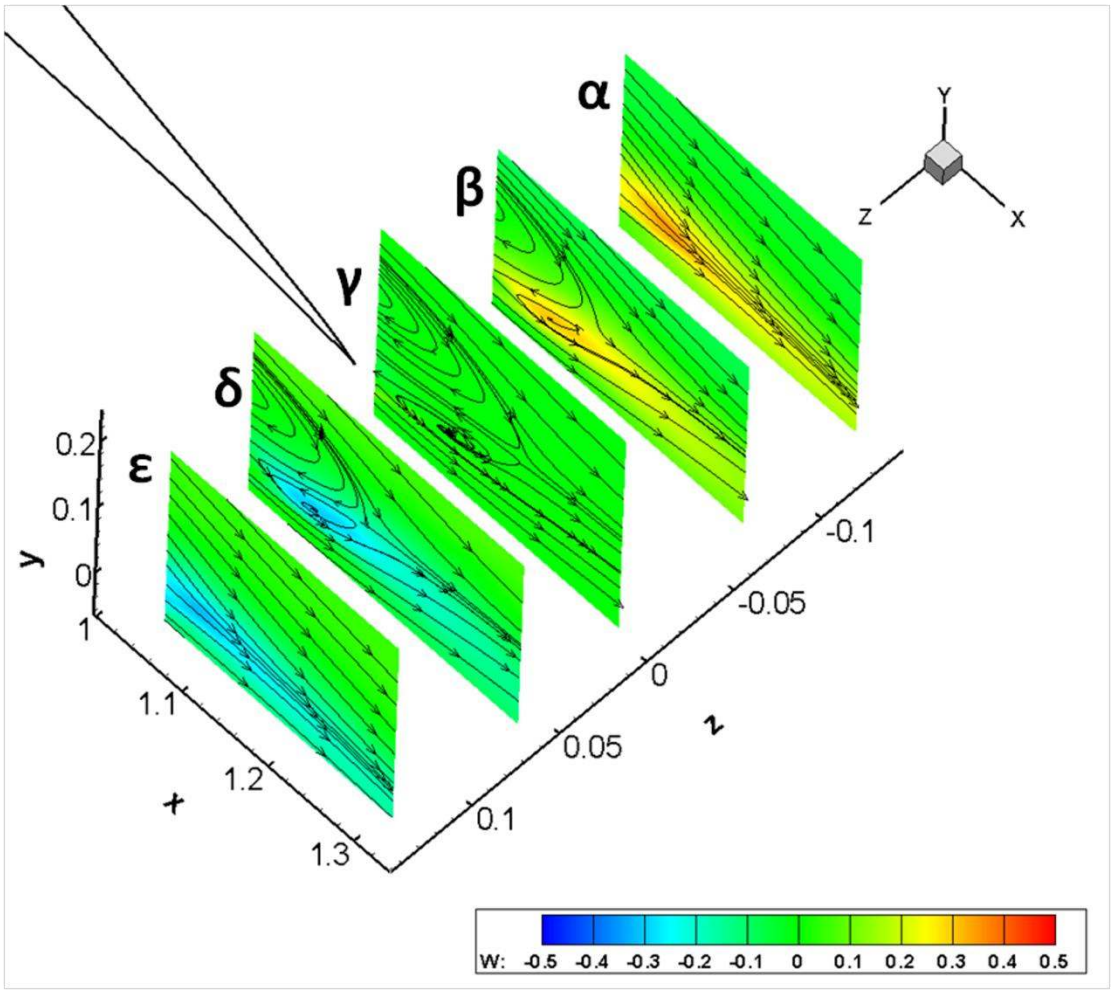

Figure 10: Contours of normalized spanwise velocity (W) at Z = 0.0 (plane γ), Z = ±0.067 (planes β and δ) and Z = ±0.133 (planes α and ε). In plane flow lines are also shown (α = 10°, Re = 0.87×10^6).

Not all profiles are exactly symmetric with respect to the centre of the wing span, which could be attributed to model imperfections regarding the wing surface or ZZ tape placement. The maximum velocity difference between profiles at either side of the midspan at any given height is 0.9m/s or $0.04U_\infty$. In any case the discrepancies are comparable to the minimum resolved velocity (0.6m/s or $0.03U_\infty$) which is the error bar value in Figure 11.

Figure 12 shows the development of the U profile along the X-axis for the spanwise locations corresponding to planes γ (mid-span), δ and ε. The profiles on planes α and β are very similar to those on planes ε and δ, respectively, and are hence not shown here. The peak velocity deficit at the two downstream locations (X = 1.18, X = 1.30) is higher compared to the relative deficit location at X = 1.06, also suggesting significant upwash induced by the SC vortices.

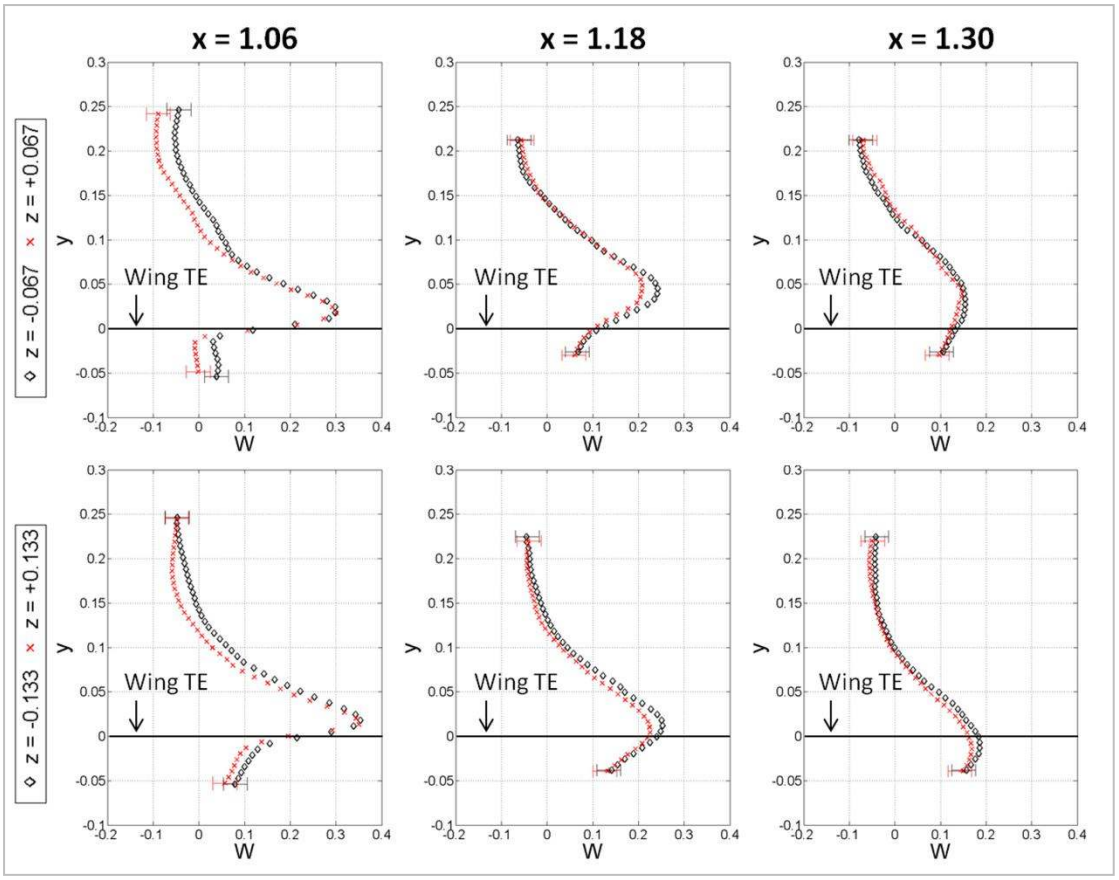

Figure 11: Spanwise velocity (W) profiles at three chordwise locations in the wake: X = 1.06 (right after the TE, first column), X = 1.18 (second column) and X = 1.30 (third column). The top and bottom row show data for Z = ±0.067 (planes β and δ) and Z = ±0.133 (planes α and ε), respectively. -W is plotted for positive Z data to facilitate comparison. Error bars equal to the minimum resolved velocity are shown only at the top and bottom of the graphs for clarity. The thick horizontal line at Y = 0.0 denotes the wing TE position (α = 10°, Re = 0.87×10^6).

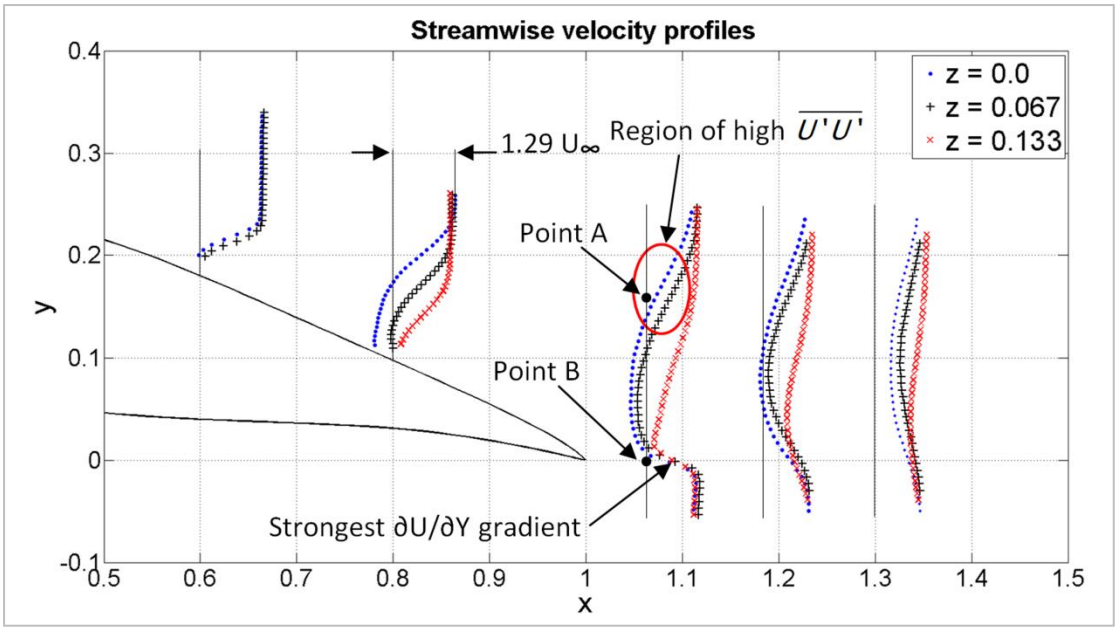

Figure 12: Normalized streamwise velocity (U) profiles at X = 0.6, 0.8, 1.06, 1.18 and 1.30. At X = 0.6 the two shown profiles correspond to Z = 0.0 (mid span) and Z = 0.067, while at all other X stations the profile at Z = 0.133 is added. The scale is the same for all curves. The vertical thin black lines correspond to U = 0 (α = 10°, Re = 0.87×10^6). Points A and B as well as the regions of high $\overline{U'U'}$ concentration and of the strongest ∂U/∂Y gradient are discussed in the Reynolds stress section.

B. The vorticity field

Figure 13 shows contours of normalized streamwise vorticity on planes A, B and C in relation to the region of reversed flow (indicated by the U = 0 isoline). On plane C, two well identified regions of vorticity are observed above the TE level (denoted as 1 and 2) and two elongated ones below them (denoted as 3 and 4). The lower placed regions 3 and 4 correspond to the spanwise shear in the wake, see also Figure 11. Each of the elongated regions has vorticity of opposite sign compared to the large region above it.

In Figure 14 (a), Q contours are shown together with in-plane velocity vectors on plane C. The areas of high Q concentrations denoted as 1 & 2 are closely located to the spanwise position of the SC foci on the wing (Z ≈ ±0.13) and are associated with the SC vortices which by the time they have reached plane C have strong X-vorticity component resulting from the streamwise alignment process (deformation) they undergo.

Two more peaks of Q appear at Z ≈ ±0.07, within the elongated regions of streamwise vorticity located underneath the SC vortices (denoted as 3 and 4). It is conceivable that these correspond to the TE vortex, at the point where it is bent away from the wing TE, inboard of the two SC vortices. This kind of curving of the TELV is clear in Figure 1 and in the Stereo - PIV data on planes normal to the wing span, which are discussed later. Note that all vortices are located outside the reversed flow region. Measurements at 7° confirm the above findings for a SC significantly smaller in size [16].

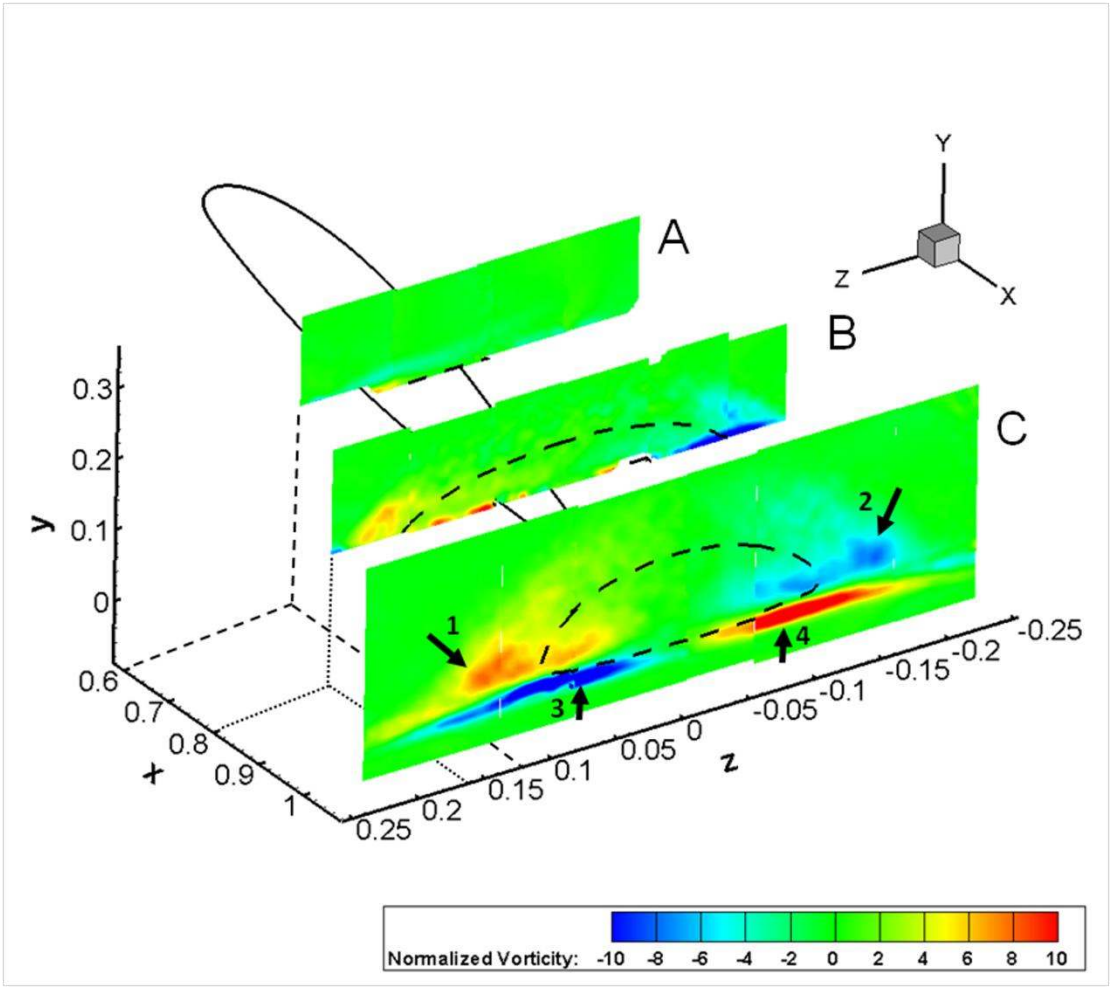

Figure 13: Contours of normalized streamwise vorticity at X = 0.6 (plane A), X = 0.8 (plane B) and X = 1.06 (plane C). The dashed iso-line corresponds to U = 0 (α = 10°, Re = 0.87×10^6).

Further insight about the positioning of the identified vortex structures can be drawn by combining the streamwise vorticity contours on plane C along with Q = 3 and $\partial U / \partial Y = \pm 4$ isolines in Figure 14 (b). The $\partial U / \partial Y = constant$ isolines can be considered as indicators of the shear layers involved, assuming that $\partial V / \partial X \approx 0$. The SC vortices appear embedded in the separation shear layer which continuous at the sides of the SC. The concentrated vortices in the lower elongated regions of vorticity are located inside the TE shear layer supporting the view that they correspond to the TE vortex, which, as already indicated, in this region will bend in a wide "U" shape (Figure 1).

Coming back to Figure 13, the two areas of opposite vorticity on plane B should not be associated with the SC vortices, since, as shown in Figure 6, plane B is located upstream of the SC vortex foci on the wing surface. These regions of vorticity correspond to the local spanwise shear.

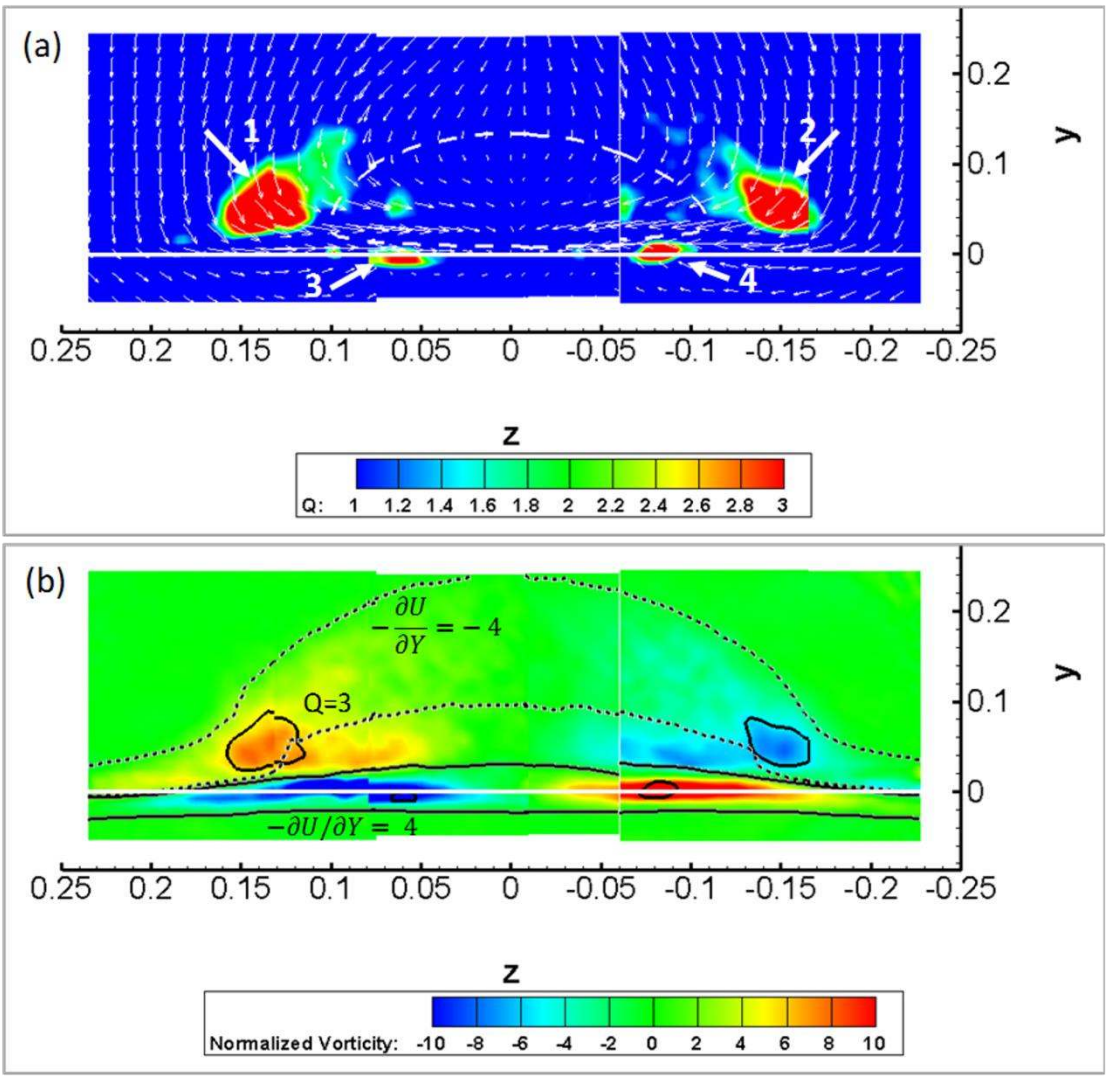

Figure 14: Contours of (a) the Q criterion with in-plane velocity vectors and U = 0 isoline. One out of every 16 vectors is plotted for clarity; (b) normalized streamwise vorticity with Q = 3 and $\partial U / \partial Y = \pm 4$ isolines at X = 1.06 (plane C). The wing TE is at Y = 0.0 and is indicated by a white horizontal line (α = 10°, Re = 0.87×10^6).

Proceeding with the spanwise development of the SLV and the TELV, Q contours plots on planes normal to the wing span are considered (Figure 15). The SLV and TELV vortices are clearly identified. On planes β, γ and δ, which lay in between the SC vortices (Z ≈ ±0.13), the SLV and TELV grow in size and strength and move higher (SLV) and downstream (TELV). The passage from plane ε-to-δ (and respectively from α-to-β) corresponds to the bending of the TELV as already discussed in connection to regions 3 and 4 in Figure 14 (a).

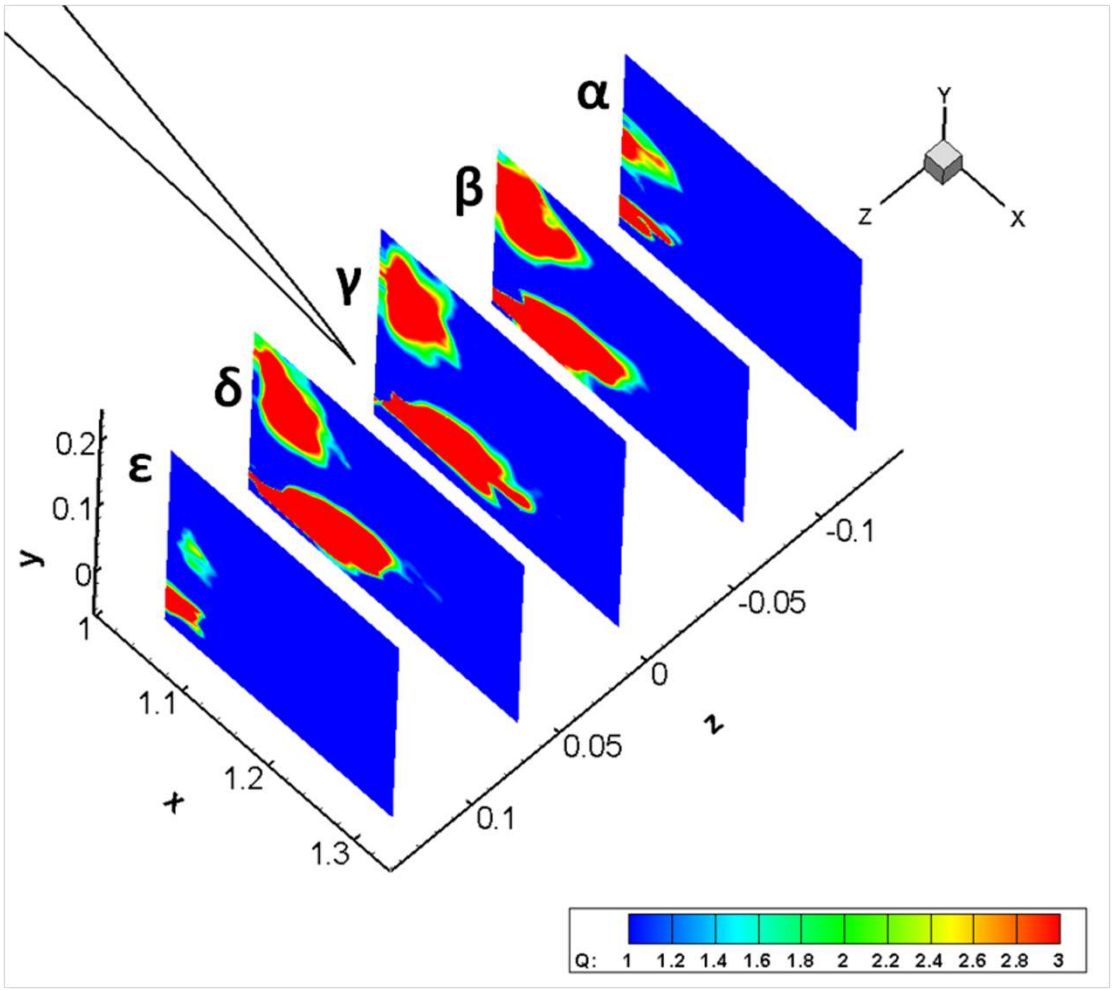

Figure 15: Contours of the Q criterion at Z = 0.0 (plane γ), Z = ±0.067 (planes β and δ) and Z = ±0.133 (planes α and ε), (α = 10°, Re = 0.87×10^6).

C. Reynolds stress data

In this section the Reynolds stresses of the averaged flow on all measured planes are presented aiming at a deeper insight in the structure of the SC. The main focus is on areas with concentration of high values. In this respect shear stresses concentrations are correlated to momentum transfer across shear layers while concentration of normal stresses are correlated to oscillatory movements of either the associated shear layer or the vortex structures in vicinity.

Normal and shear Reynolds stress distributions on all planes are shown in Figure 16 to Figure 18 and Figure 19 to Figure 21, respectively. Normal stresses have significant anisotropy; their values are in general an order of magnitude higher than the shear stresses; $\overline{U'U'}$ is in general more intense compared to the other components, while $\overline{W'W'}$ remains in all areas smaller in value.

In addition to the identified vortex structures, the flow features two spanwise shear layers encompassing the SC. As expected and confirmed in Figure 19, the concentration of the $\overline{U'V'}$ shear stress taking care of momentum transfer is high within the shear layers. The absolute maximum $\overline{U'V'}$ values are almost two times higher than the other shear stresses

values. Figure 19 also clearly indicates the separation shear layer growth in height as it develops downstream. In fact the peak values of $\overline{U'V'}$ on planes β - δ are significantly higher compared to planes α and ε, signifying the growth of the SLV (see also Figure 15). On planes α and ε the lower intensity, as well as the gradual fading in the wake, indicate the spanwise limits of the reversed flow pocket as detected in Figure 13. Over the lower part of the all planes in Figure 19, the areas of high positive $\overline{U'V'}$ are associated with the TE shear layer. Again there is higher concentration on planes β - δ signifying the growth of the TELV in that region.

The top regions of high $\overline{U'V'}$ concentration coincide with those of high $\overline{U'U'}$ Reynolds stress concentration, see Figure 16. The fact that the highest values of $\overline{U'U'}$ do not appear where ∂U/∂Y is strongest (i.e. at the TE shear layer, see Figure 12), but at the separation shear layer, where ∂U/∂Y is not as significant, suggests that a different physical mechanism exists which leads to substantial deviations of U, other than intense shear. Individual Stereo PIV snapshots show that the location of the separation shear layer (and the reversed flow region) varies considerably in time, significantly more than the TE shear layer location does. Previous studies [3], [19] also mention a flapping motion of the shear layer associated with SCs and link it to low frequency oscillations. No frequency analysis can be performed from the present data, but this motion conceivably is the cause of the strong U variations.

Consider two fixed points in space at X = 1.06, for simplicity at the centre of the wing span (Z = 0.0). Let one be inside the separation shear layer right above the reversed flow region at Y = 0.16 (point A in Figure 12 and Figure 16) and the other inside the TE shear layer at Y = 0.0 (point B in Figure 12 and Figure 16) where the maximum value of ∂U/∂Y is observed. As the separation shear layer performs a relatively large movement in the vertical direction the streamwise velocity at point A will vary significantly in time, being sometimes at regions of high U (well outside the reversed flow region) and sometimes at regions of negative U (inside the reversed flow region). On the contrary, the TE shear layer is more stable and, as a result, U at point B varies less in time despite being in a region of stronger ∂U/∂Y.

Intense $\overline{V'V'}$ activity (Figure 17) starts to appear downstream of the TE on plane C and, mainly, in the wake on planes α - ε. It is conceivable that areas of high $\overline{V'V'}$ values appearing in proximity to vortices parallel to the X axis (here the SC vortices) indicate fluctuation of the vortices in the Z direction [32]. Interestingly, regions of high $\overline{V'V'}$ on planes β and δ start right after the reversed flow region ends (see in plane flow lines in Figure 17-b), indicating that the SC vortices move inboard as the reversed flow region width decreases. Less intense but clearly visible $\overline{V'V'}$ activity within the separated shear layer on plane C is associated to the flapping of the layer.

Regions of high $\overline{W'W'}$ (Figure 18) indicate fluctuation in the Y direction [32]. These regions appear further downstream of the wing TE (at X ≈ 1.16) and not directly after it, which is again attributed to the inboard movement of the SC vortices downstream of the wing TE as indicted by CFD. The fact that $\overline{W'W'}$ values are small compared to $\overline{V'V'}$ values, suggests that the vertical movement of the SC vortices is smaller than their spanwise wandering.

On plane C (Figure 20-a) two antisymmetric areas of high $\overline{V'W'}$ values are centered along the U = 0 isoline and inboard of the SC vortices that lay outside the reversed flow region (see Figure 14). The regions are circular and have a horizontal "tail", indicated by arrows in Figure 20-a. Study of the Reynolds stress production terms (not included here) shows that production of $\overline{V'W'}$ (P_{vw}) peaks at the region of the tails (Figure 22), which suggests transport from the region where $\overline{V'W'}$ is produced towards the circular regions of high $\overline{V'W'}$ carried out by the SC vortices. The production term P_{vw} is computed according to equation (4) below, where variations in the chordwise direction are considered small:

$$P_{vw} = -\overline{V'V'}\frac{\partial W}{\partial Y} - \overline{V'W'}\frac{\partial W}{\partial Z} - \overline{V'W'}\frac{\partial V}{\partial Y} - \overline{W'W'}\frac{\partial V}{\partial Z} \qquad (4)$$

Equally high $\overline{V'W'}$ activity is also found in the wake (Figure 20-b) further inboard on planes δ and β which appears as a continuation of the regions shown on plane C. These regions in the wake start just after the end of the reversed flow pocket, as indicated by the in-plane flow lines. On plane C intense $\overline{V'W'}$ activity is linked to a region of strong shear strain between the SC vortices and the reversed flow region which extends downstream in the wake, beyond the reversed flow region.

The $\overline{U'W'}$ shear stress distribution in Figure 21 has lower peaks than the other shear stresses. The peaks on plane B and C (Figure 21-a) appearing outside of the reversed flow region, are linked to the spanwise shear of U and the flow curvature as the flow circumvents the separation bubble. On plane C and subsequently on the planes in the wake (Figure 21-b), regions of peak $\overline{U'W'}$ values appearing in the lower parts of the measuring windows are correlated to spanwise vorticity shown in Figure 15.

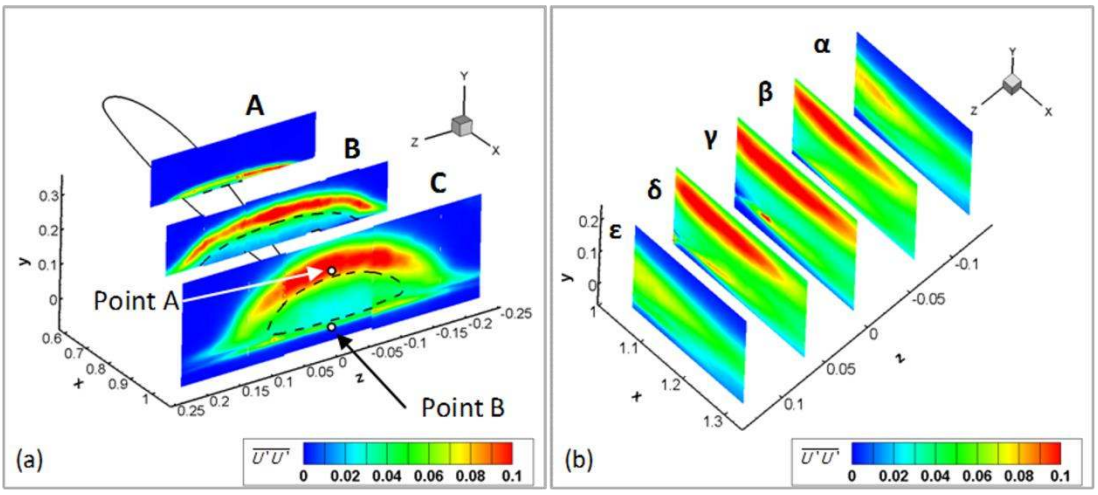

Figure 16: Contours of the $\overline{U'U'}$ Reynolds stress (a) at planes normal to the flow, at X = 0.6, 0.8 and 1.06; Points A (1.06, 1.6, 0) and B (1.06, 0, 0) are also indicated. (b) at planes normal to the wing span, at Z = 0.0, Z = ±0.067 and Z = ±0.133. The dashed iso-line on planes A, B and C corresponds to U = 0 (α = 10°, Re = 0.87×10^6).

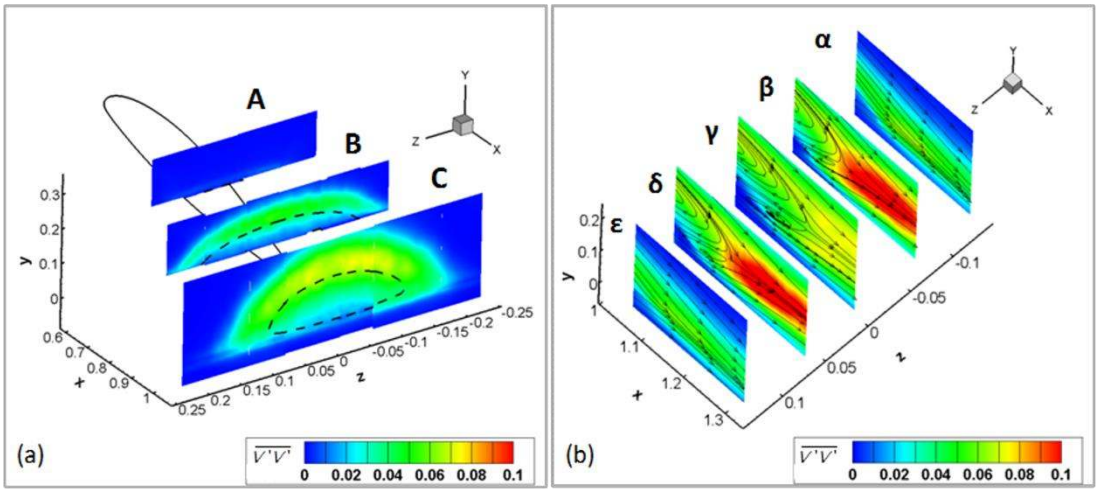

Figure 17: Contours of the $\overline{V'V'}$ Reynolds stress (a) at planes normal to the flow, at X = 0.6, 0.8 and 1.06; (b) at planes normal to the wing span, at Z = 0.0, Z = ±0.067 and Z = ±0.133, with in plane flow lines. The dashed iso-line on planes A, B and C corresponds to U = 0 (α = 10°, Re = 0.87×10^6).

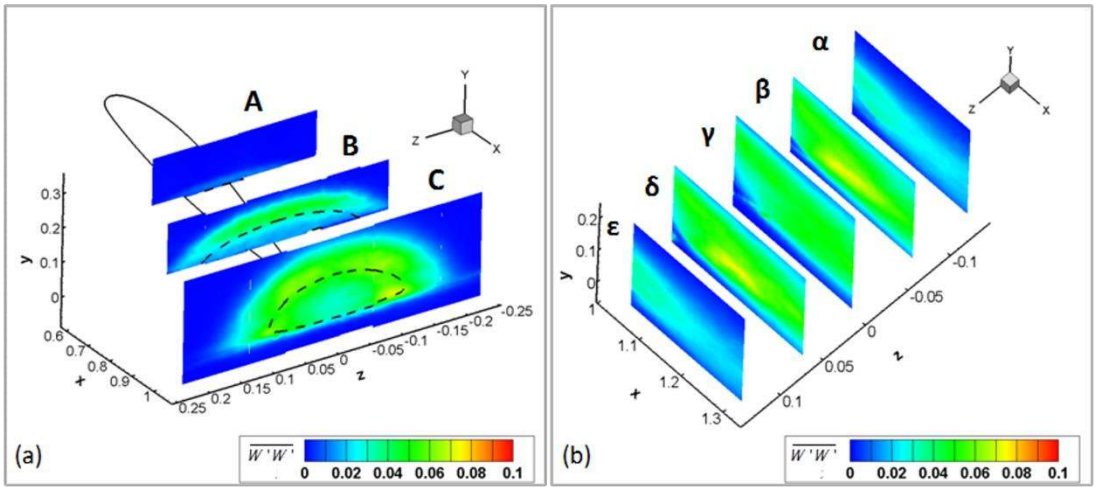

Figure 18: Contours of the $\overline{W'W'}$ Reynolds stress (a) at planes normal to the flow, at X = 0.6, 0.8 and 1.06; (b) at planes normal to the wing span, at Z = 0.0, Z = ±0.067 and Z = ±0.133. The dashed iso-line on planes A, B and C corresponds to U = 0 (α = 10°, Re = 0.87×10^6).

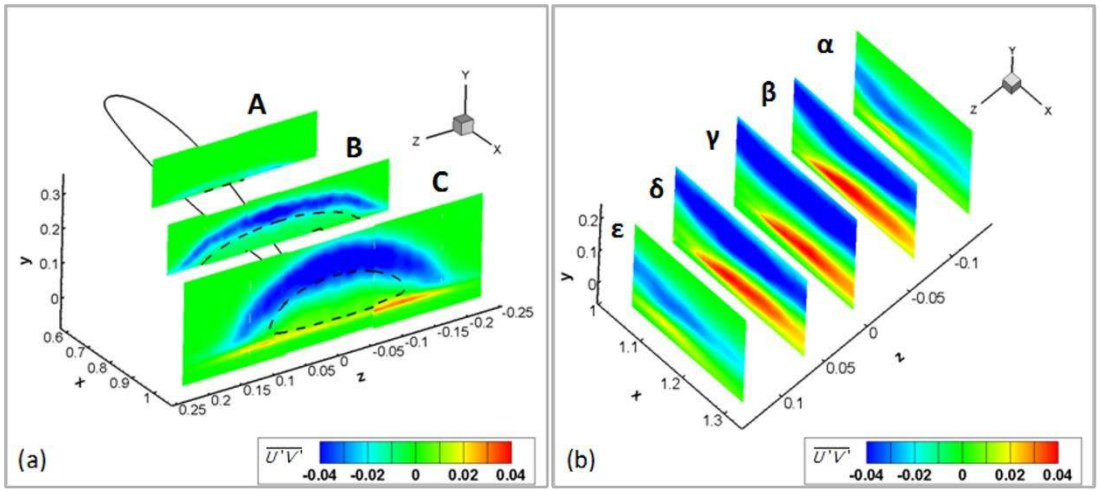

Figure 19: Contours of the $\overline{U'V'}$ Reynolds stress (a) at planes normal to the flow, at X = 0.6, 0.8 and 1.06; (b) at planes normal to the wing span, at Z = 0.0, Z = ±0.067 and Z = ±0.133. The dashed iso-line on planes A, B and C corresponds to U = 0 (α = 10°, Re = 0.87×10^6).

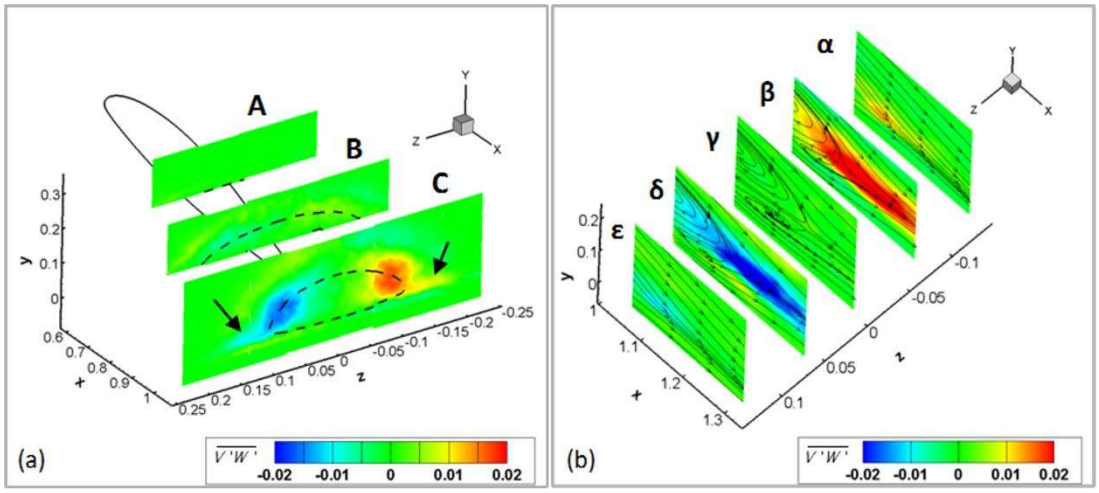

Figure 20: Contours of the $\overline{V'W'}$ Reynolds stress (a) at planes normal to the flow, at X = 0.6, 0.8 and 1.06; (b) at planes normal to the wing span, at Z = 0.0, Z = ±0.067 and Z = ±0.133 with in plane flow lines. The dashed iso-line on planes A, B and C corresponds to U = 0 (α = 10°, Re = 0.87×10^6).

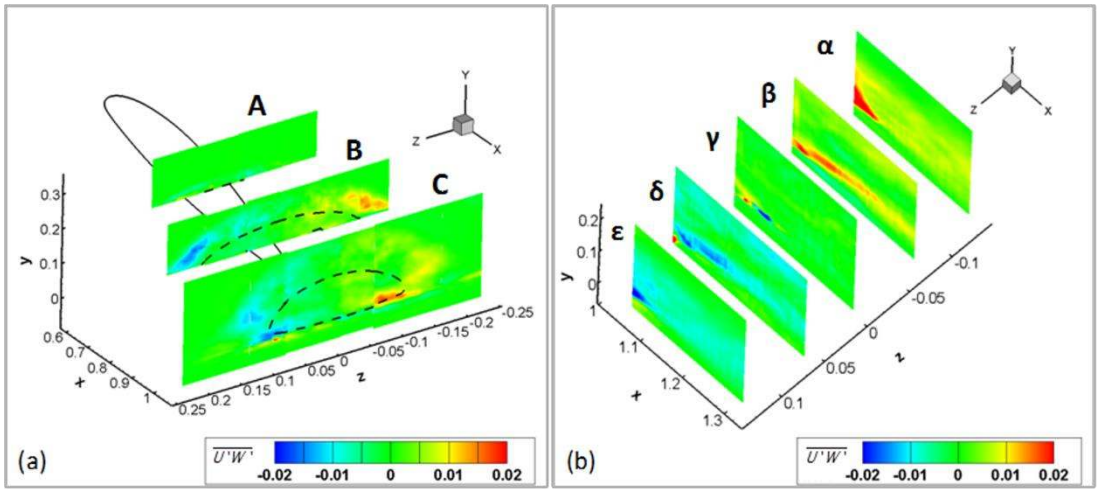

Figure 21: Contours of the $\overline{U'W'}$ Reynolds stress (a) at planes normal to the flow, at X = 0.6, 0.8 and 1.06; (b) at planes normal to the wing span, at Z = 0.0, Z = ±0.067 and Z = ±0.133. The dashed iso-line on planes A, B and C corresponds to U = 0 (α = 10°, Re = 0.87×10^6).

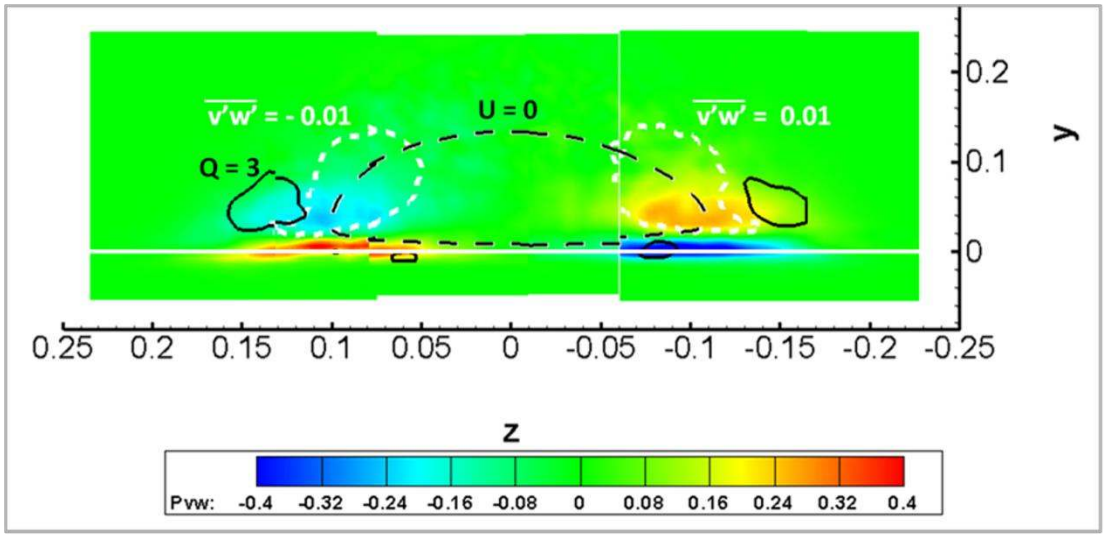

Figure 22: Contour of the $\overline{V'W'}$ Reynolds stress production term (Pvw) at X = 0.6 (plane C). The white dashed iso-line corresponds to $\overline{V'W'}$ = ±0.01, the black dashed iso-line corresponds to U = 0 and the black continuous iso-line corresponds to Q = 3. The wing TE is at Y = 0.0 and is indicated by a white horizontal line (α = 10°, Re = 0.87×10^6).

D. In relation to CFD results

In [15] 3D RANS simulations showed a delay of ~3° in predicting the onset of the SC which numerically occurred at α = 9°. At all angles of attack, a SC was formed having the same structure as the one shown in Figure 1. While it is expected that at the incidence here considered (α = 10°) the amount of separation will be smaller compared to the experimentally observed, a comparison between CFD and wind tunnel data is still legitimate in order to specify the origin of this difference and assess the quality of the predictions with respect to flow field characteristics.

In Figure 23 measured and simulated streamwise velocity and vorticity contour plots on plane C are compared. On the CFD side, spanwise vorticity iso-lines for ω_z = -4 (dashed lines)

and ω_z = 4 (solid lines) are drawn. The strips defined by each pair of lines enclose the separation shear layer and the TE shear layer, respectively. On the Stereo PIV side, $\partial U / \partial Y = \pm 4$ isolines are drawn for the same reason, as explained earlier. In both measurements and CFD, vorticity is a derived quantity and therefore the values obtained will depend on the grid resolution. Since the grids are substantially different, the two sets of values are not directly comparable, however, the general shape and trends are. The agreement appears good. CFD captures the main shape of the wake although the SC is smaller in size. In particular, the reversed flow region is smaller and the SC vortex appears slightly more inboard than in the Stereo-PIV data. The SC vortices are embedded in the separated shear layer and the elongated concentrations of vorticity that result from the deformation of the TELV are present and embedded in the TE shear layer. Predictions of similar quality (not shown here) were also obtained on the measurement planes in the wake. In summary it follows that 3D RANS simulations produce the same flow pattern as in the measurements but quantitatively under-predict certain flow characteristics.

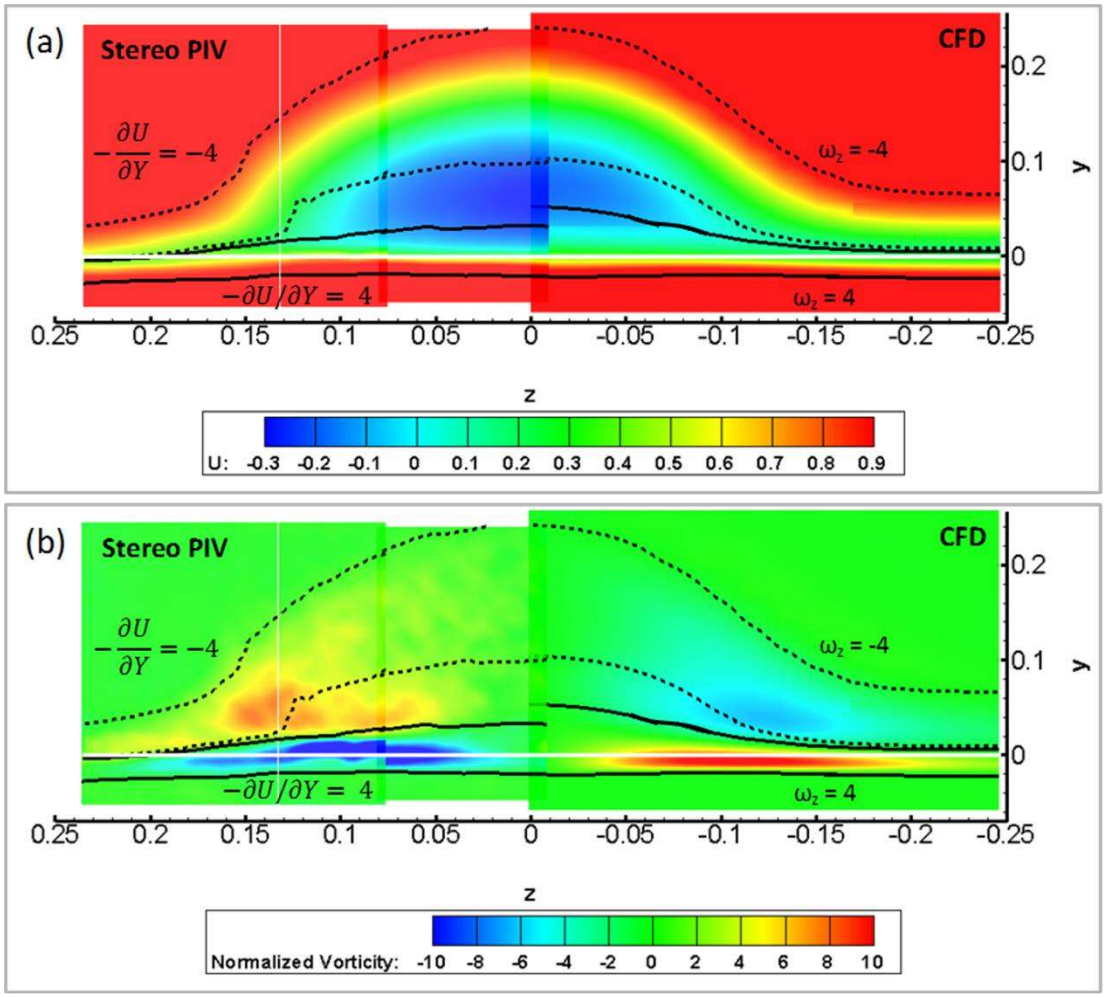

Figure 23: Contours of (a) normalized streamwise velocity (U) and (b) normalized streamwise vorticity at X = 1.06 (plane C). Stereo PIV (left) and CFD data (right). On the CFD data, iso-lines of normalized spanwise vorticity are drawn for ω_z = -4 (dashed lines) and ω_z = 4 (solid lines) indicating the strips corresponding to the separation and the TE shear layer respectively. On the Stereo PIV data iso-lines of $\partial U / \partial Y = \pm 4$ are accordingly drawn. The wing TE is at Y = 0.0 and is indicated by a white horizontal line.

As detailed in the previous section the turbulence characteristics of the flow inside a SC are highly anisotropic and the Boussinesq approximation, underlying all eddy viscosity models is invalid (see also [16]). In this sense the qualitative agreement, on a time averaged level, between the experiments and the eddy viscosity simulations may seem surprising. In fact, the normal stresses are indeed wrongly predicted both in terms of values and profile shape as Figure 24 (a) shows for $\overline{U'U'}$. Negative values are allowed, which is not uncommon in eddy viscosity turbulence models. As regards shear stresses, while their prediction significantly deviates from measurements, the shape of the predicted profile follows the experimental trend as shown in Figure 24 (b) for $\overline{U'V'}$.

In RANS simulations it is important to correctly predict at least the trend of the shear stresses since they transport momentum. The situation with normal stresses is different. Normal stresses act as pressure terms. Being orders of magnitude smaller than the actual pressure terms, their significance to the development of the flow is smaller. It is therefore conceivable that this is the reason the present CFD results are qualitatively close to the experimental data.

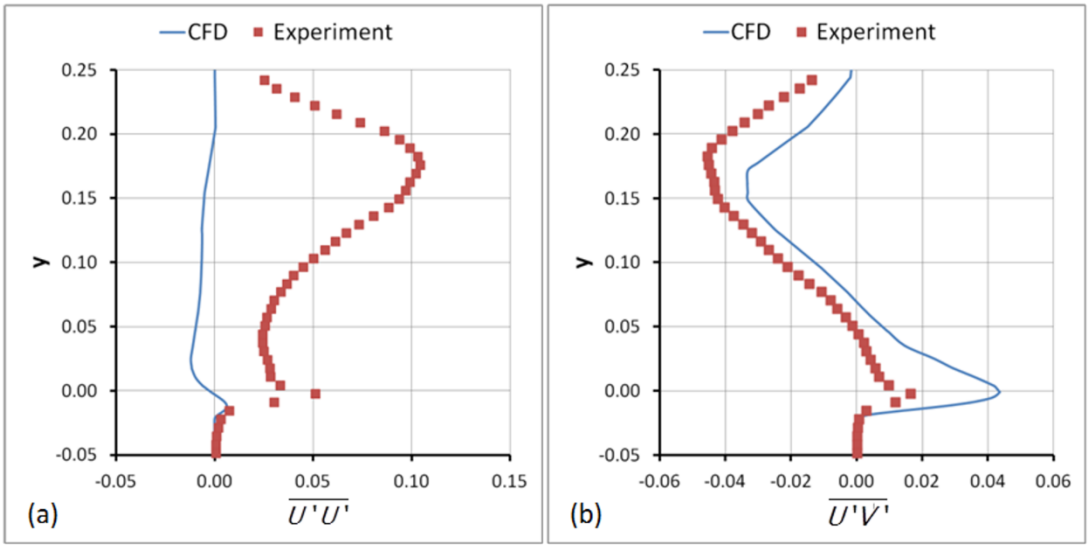

Figure 24: (a) $\overline{U'U'}$ and (b) $\overline{U'V'}$ variation along the vertical axis at the center of the SC (Z = 0) as measured in the wind tunnel and predicted by CFD using the Spalart-Allmaras eddy viscosity turbulence model.

IV. SYNTHESIS AND CONCLUSIONS

The present work analyzes the structure of a SC formed on a wing model at Re = 0.87×10^6 and $\alpha = 10^o$. The analysis is based on Stereo PIV flow measurements which are combined with 3D eddy viscosity RANS data. The inherent unsteadiness of SCs at this Reynolds number was suppressed by placing a ZZ tape at the LE covering 10% of the model span at its center which stabilized the flow and led to a single SC at the center of the model. Both the numerical and the wind tunnel data presented here concern the time-averaged flow, after SC formation is concluded, and hence no conclusions regarding the formation mechanism can be drawn. The comparison between tests and RANS simulations showed that the specific CFD modeling predicts the same flow pattern and is in good qualitative agreement with the

experimental results. By combining the two sets of data, a consistent description of the time averaged flow was given which in this section is compared to previously suggested models.

The SC as a whole emerges in between the separation and TE shear layers. Three types of vortex structures were identified that remain within the SC: The pair of counter rotating Stall Cell vortices, the Separation Line Vortex and the Trailing Edge Line Vortex.

The SC vortices start normal to the wing suction surface with their focal points within the area defined by the separation line. The former derives from the CFD data while the latter derives from both CFD and flow visualization. Both measurements and CFD indicate that the SC vortices quickly bend in the streamwise direction and are subsequently convected in the wake as trailing vortices. The SC vortices remain embedded in the separation shear layer but outside the region of reversed flow while over the wing surface but also in the wake. In the wake they approach each other and, being counter rotating, they are pushed upwards under mutual induction.

The Separation and TE line vortices run parallel to the TE. They both grow significantly over the center and between the SC vortices where the TELV takes an open “U” shape while the SLV takes an open “∩” shape.

Under the effect of the upwash generated by the SC vortices the separation shear layer is pushed upwards and the cross section of the SC grows in height while above the wing. Downstream of the TE, it contracts in the spanwise direction and gets smaller in width compared to the width of the SC on the wing.

While the above description agrees in several aspects with the previously suggested models in [3] and [20], there are some differences. Yon & Katz [3] claimed that no concentrated spanwise vortices exist and that the SC vortices "bound" the separation shear layer, while Rodriguez & Theofilis [20] state that the separation line vortex breaks and continues downstream. The flow field measurements presented in this study show that the SC vortices are embedded in the separation shear layer while both the SLV and the TELV are concentrated vortices which extend parallel to the wing TE outboard of the SC. The latter means that flow can remain separated outside the SC.

It should be noted at this point that the model suggested in [3] was based on surface pressure measurements and single point wake pressure data, while the model in [20], on one hand, refers to very low Re numbers and, on the other, is based on stability analysis of a spanwisely disturbed 2D steady flow. In this sense the data on which the present SC structure description is based is more complete. The analysis is supported by flow field measurements within the SC, which provide the first reconstruction of all the mean flow vortical structures inside a SC. In addition good agreement is found between tests and CFD results with respect to the type and position of vortex structures as well as the main underlying interactions.

With respect to turbulence characteristics, both normal and shear Reynolds stresses are highly anisotropic. Concentrations of high normal Reynolds stresses in the separated shear layer and along the SC vortices indicate the presence of fluctuations, more specifically the

flapping of the separation shear layer and the wandering of the SC vortices in space. Streamwise shear Reynolds stresses $\overline{U'V'}$ and $\overline{U'W'}$ are connected to momentum transfer across the shear layers, while cross shear stress $\overline{V'W'}$ is correlated to vortex deformation.

In both [3] and [19], low frequency (St << 0.1) pressure fluctuations were observed, measured on or close to the wing surface. Yon & Katz [3] link these to large amplitude shear layers motions, while Elimelech et al. [19] state that the SCs respond to the low frequency perturbations by changing their thickness and boundaries. In agreement with both of the above statements the presently reported Stereo PIV data indicate such a motion, which justifies the presence of high $\overline{U'U'}$ values in the separated shear layer encompassing the SC.

It is legitimate to question certain aspects of the present analysis. The SC was artificially stabilized and the CFD predictions were not quantitatively accurate. As explained in Section II and detailed in [14] the stabilized flow corresponds to the undisturbed one for a high enough angle of attack, in terms of SC size at least. Then as regards the numerical simulations, the use of an eddy viscosity model is certainly a compromise for such an anisotropic flow. Still, since RANS modeling is the one most used in practice, its limits should be known and clear. Besides, previous studies showed that the choice of eddy viscosity model is not crucial [17], [18], while DES do not always provide better results [6]. Based on both the current study and previous investigations LES modeling is a particularly recommended option which we did not pursued due to limitations in computer capacity.

ACKNOWLEDGEMENTS

Dr Stamatios Pothos (TSI Incorporated, USA) is gratefully acknowledged for his guidance throughout the experimental part of this paper.

The authors would like to thank Onassis Foundation for their support through the G ZF 032 / 2009-2010 scholarship grant.

REFERENCES

[1] N. Gregory, V. Quincey, C. O'Reilly, and D. Hall, "Progress Report on Observations of Three-Dimensional Flow Patterns obtained during Stall Development on Aerofoils, and on the Problem of Measuring Two-Dimensional Characteristics," London, #C.P. 1146 Her Majesty's Stationery Office, 1971.

[2] A. Winkelmann and J. Barlow, "Flowfield Model for a Rectangular Planform Wing beyond Stall," *AIAA*, vol. 18, no. 08, pp. 1006–1008, 1980.

[3] S. Yon and J. Katz, "Study of the Unsteady Flow Features on a Stalled Wing," *AIAA J.*, vol. 36, no. 3, pp. 305–312, 1998.

[4] G. Schewe, "Reynolds-number effects in flow around more-or-less bluff bodies," *J. Wind Eng. Ind. Aerodyn.*, vol. 89, pp. 1267–1289, Dec. 2001.

[5] C. M. Velte and M. O. L. Hansen, "Investigation of flow behind vortex generators by stereo particle image velocimetry on a thick airfoil near stall," *Wind Energy*, Jul. 2012.

[6] F. Bertagnolio, N. N. Sørensen, and J. Johansen, *Profile catalogue for airfoil sections based on 3D computations*. 2006.

[7] A. P. Broeren and M. B. Bragg, "Spanwise Variation in the Unsteady Stalling Flowfields of Two-Dimensional Airfoil Models," *AIAA J.*, vol. 39, no. 9, pp. 1451–1461, 2001.

[8] G. A. Flynn, J. F. Morrison, and D. G. Mabey, “Buffet Alleviation on Swept and Unswept Wings at High Incidence,” *J. Aircr.*, vol. 38, no. 2, pp. 368–378, Mar. 2001.
[9] J. B. Barlow, W. H. Rae, and A. Pope, *Low-speed wind tunnel testing*. New York [etc.]: John Wiley & Sons, 1999.
[10] J. Supamusdisukul, “Experimental investigation of wing-fuselage interaction geometries including CFD analyses.,” MSc Thesis, University of Maryland, MAryland, US, 2008.
[11] G. F. Moss and P. M. Murdin, *Two-Dimensional Low-Speed Tunnel Tests on the NACA 0012 Section Including Measurements Made During Pitching Oscillations at the Stall*, 1. ed. London: H.M. Stationery Office, 1971.
[12] P. Fuglsang and S. Bove, “Wind Tunnel Testing Of Airfoils Involves More Than Just Wall Corrections,” presented at the European Wind Energy Conference, Brussels., 2008.
[13] N. N. Sørensen and S. Schreck, “Computation of the National Renewable Energy Laboratory Phase-VI rotor in pitch motion during standstill,” *Wind Energy*, vol. 15, no. 3, pp. 425–442, Apr. 2012.
[14] M. Manolesos and S. G. Voutsinas, “Geometrical characterization of stall cells on rectangular wings,” *Wind Energy*, May 2013.
[15] M. Manolesos, G. Papadakis, and S. G. Voutsinas, “Experimental and computational analysis of stall cells on rectangular wings,” *Wind Energy*, Apr. 2013.
[16] M. Manolesos, “Experimental and computational investigation of three-dimensional separation and separation control using passive vortex generators,” PhD Thesis, NTUA, Athens, 2013.
[17] R. Wokoeck, N. Krimmelbein, J. Ortmanns, V. Ciobaca, R. Radespiel, and A. Krumbein, “RANS Simulation and Experiments on the Stall Behaviour of an Airfoil with Laminar Separation Bubbles,” 2006.
[18] T. Zarutskaya and R. Arieli, “On Vortical Flow Structures at Wing Stall and Beyond,” AIAA Paper 2005-4913, 2005.
[19] Y. Elimelech, R. Arieli, and G. Iosilevskii, “The three-dimensional transition stages over the NACA-0009 airfoil at Reynolds numbers of several ten thousand,” *Phys. Fluids*, vol. 24, no. 2, p. 024104, 2012.
[20] D. Rodríguez and V. Theofilis, “On the birth of stall cells on airfoils,” *Theor. Comput. Fluid Dyn.*, vol. 25, no. 1–4, pp. 105–117, Mar. 2010.
[21] F. Bertagnolio, N. N. Sørensen, and F. Rasmussen, “New Insight Into the Flow Around a Wind Turbine Airfoil Section,” *J. Sol. Energy Eng.*, vol. 127, no. 2, p. 214, 2005.
[22] F. R. Menter, “Zonal two-equation k-w turbulence model for aerodynamic flows,” *AIAA Pap.*, vol. 1993–2906, 1993.
[23] P. R. Spalart and S. R. Allmaras, “A One-Equation Turbulence Model for Aerodynamic Flows,” AIAA Paper 92-0439, 1992.
[24] D. C. Wilcox, *Turbulence modeling for CFD*, 2nd ed. La Cãnada, Calif: DCW Industries, 1998.
[25] K. Taira and T. Colonius, “Three-dimensional flows around low-aspect-ratio flat-plate wings at low Reynolds numbers,” *J. Fluid Mech.*, vol. 623, p. 187, Mar. 2009.
[26] D. Weihs and J. Katz, “Cellular patterns in poststall flow over unswept wings,” *AIAA J.*, vol. 21, no. 12, pp. 1757–1759, Dec. 1983.
[27] J. C. R. Hunt, A. A. Wray, and P. Moin, “Eddies, streams, and convergence zones in turbulent flows,” Center for Turbulence Research Report CTR-S88, 1988.
[28] J. Jeong and F. Hussain, “On the identification of a vortex,” *J. Fluid Mech.*, vol. 285, no. 1, pp. 69–94, 1995.
[29] D. Mourikis, V. Riziotis, and S. G. Voutsinas, “Aerodynamic design using genetic algorithms and application to rotor blades,” presented at the International Conference

on Computational and Experimental Engineering and Sciences, Madeira, Portugal, 2004.
[30] J. Westerweel, “Theoretical analysis of the measurement precision in particle image velocimetry,” *Exp. Fluids*, vol. 29, no. 1, pp. S003–S012, 2000.
[31] J. M. Foucaut, B. Miliat, N. Perenne, and M. Stanislas, “Characterization of different PIV algorithms using the EUROPIV synthetic image generator and real images from a turbulent boundary layer,” in *Particle Image Velocimetry: Recent Improvements*, Springer, 2004, pp. 163–185.
[32] K. P. Angele and F. Grewe, “Instantaneous Behavior of Streamwise Vortices for Turbulent Boundary Layer Separation Control,” *J. Fluids Eng.*, vol. 129, no. 2, p. 226, 2007.